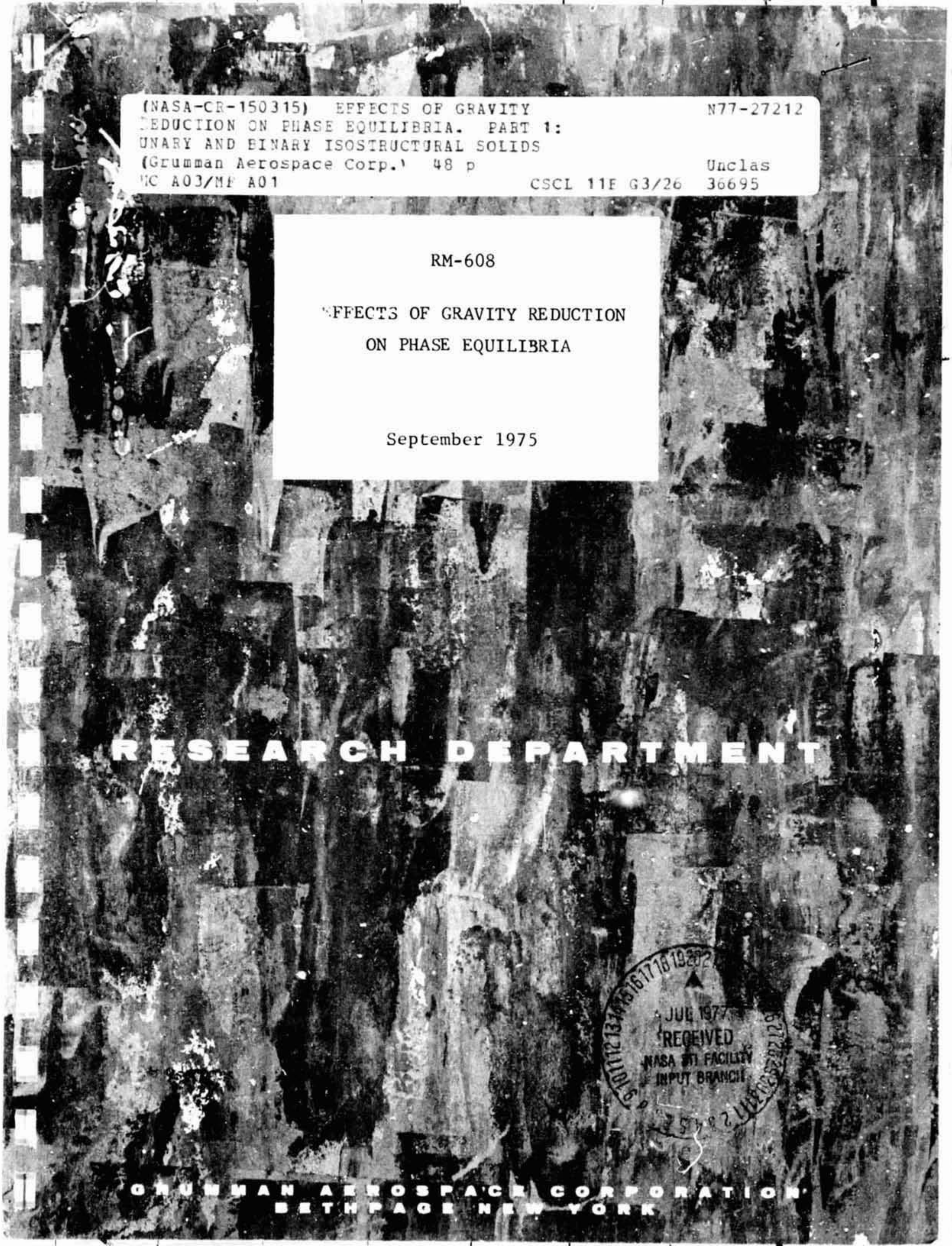

RM-608

EFFECTS OF GRAVITY REDUCTION ON PHASE EQUILIBRIA

September 1975

RESEARCH DEPARTMENT

GRUMMAN AEROSPACE CORPORATION
BETHPAGE NEW YORK

EFFECTS OF GRAVITY REDUCTION
ON PHASE EQUILIBRIA

Part 1 - Unary and Binary Isostructural Solids

RM-608

Prepared for

George C. Marshall Space Flight Center
Marshall Space Flight Center
Alabama 35812

September 1975

This investigation was partially funded by the
National Aeronautics and Space Administration
under Contract NAS8-28728

D. J. Larson, Jr.

Research Department
Materials and Structural Mechanics
Grumman Aerospace Corporation
Bethpage, New York 11714

Approved by:
Charles E. Mack, Jr.
Director of Research

ABSTRACT

Analysis of the Skylab II M553 Experiment samples resulted in the hypothesis that the reduced gravity environment was altering the melting and solidification reactions. The present theoretical study was conducted to define the conditions under which such alteration of phase relations is feasible, determine whether it is restricted to space processing, and, if so, ascertain which alloy systems or phase reactions are most likely to demonstrate such effects.

This memorandum considers phase equilibria of unary and binary systems with a single solid phase (unary and isomorphous). Subsequent investigations will deal with more complex systems, which will be described in our Part 2 memorandum.

TABLE OF CONTENTS

LIST OF SYMBOLS

g	- gravitational level	(cm/sec^2)
m	- mass	(gm)
P_t	- total local pressure	(mm Hg)
P_h	- hydrostatic pressure	(mm Hg)
P_γ	- surface tension pressure	(mm Hg)
P_e	- environmental pressure	(mm Hg)
P_{tv}	- total local pressure in a vacuum	(mm Hg)
δ	- specific weight	(g/cm^3)
h	- height of liquid above the point of interest	(cm)
γ	- surface tension	(dyne/cm)
R_o	- maximum sphere radius	(cm)
R	- radius from sphere center to point of interest	(cm)
ϕ	- see Fig. 4	
θ	- solid/liquid contact angle	(degrees)
T	- temperature	(K)
ΔH_f	- enthalpy of fusion	(cal/g-atom)
ΔV_f	- volume change of fusion	(cm^3/g-atom)
T_{vp}	- temperature at the vaporization point	(K)
dT	- temperature change	(K)
L_I	- liquid one	
L_{II}	- liquid two	
α	- solid rich in component A	
β	- solid rich in component B	
G	- gas	
L_{III}	- liquid three	
Q	- triple point	
H	- quadruple point	

LIST OF SYMBOLS (Continued)

GL - gas-liquid equilibrium curve
$G\alpha$, $G\beta$ - gas-solid equilibrium curve
$L\alpha$, $L\beta$ - liquid-solid equilibrium curve
P-T-X - pressure-temperature-composition diagram
T-X - temperature-composition (isobaric) section
P-T - pressure-temperature projection
P_1 - total internal pressure at one-g (mm Hg)
P_o - total internal pressure at zero-g (mm Hg)
P_{QA} - pressure at the triple point of A (mm Hg)
T_{mA} - temperature at the melting point of A (K)
T_{QA} - melting point at the triple point of A (K)
T_1 - temperature at one-g (K)
T_o - temperature at zero-g (K)
ΔP_a - pressure reduction, for case a, on going isotnermally from one-g to low-g
ΔP_b - pressure reduction, for case b, on going isothermally from one-g to low-g
ΔT_a - temperature increment between test temperature and GL_A curve for case a
ΔT_b - temperature increment between test temperature and GL_A curve for case b
C_m - liquid/liquid critical point at minimum temperature, maximum pressure
C_p - liquid/liquid critical point at maximum temperature, minimum pressure
"flexing" - Maxima or minima in $GL\alpha$ lines in P-T space

INTRODUCTION

There is little doubt that exploration of the orbital low-g environment will lead to new products. Past experience has shown that every new working environment that has been discovered and explored has resulted in new products based on the new technology. At the time a new environment is discovered or becomes readily accessible, investigators usually find it difficult to predict the kinds of products that will eventually result. This is because the environment has not been fully characterized, investigators have not experienced it first hand, nor have the processes of research, development, and pilot-plant operations yet matured. Most useful products stem from this sequence rather than from strictly theoretical considerations.

On the basis of our first-hand experience with Skylab II experiments, we have characterized the low-g environment in terms of the phase reactions and phase diagrams fundamental to all materials processing, and we anticipate immediate benefits to scientists intending to work with the low-g environment.

This memorandum summarizes our analysis of altered phase equilibria in low-g for simple systems. A subsequent memorandum (Part 2) will complete the phase diagram analysis for more complex systems and consider potential applications to processes and products.

ANALYTICAL RESULTS AND DISCUSSION

BACKGROUND

The Skylab II M553 Containerless Melting and Solidification Experiment revealed macroscopic distortions in some of the orbitally processed samples (Fig. 1), whereas similarly processed samples of different composition exhibited the anticipated (Ref. 1) high degree of spherical symmetry (Fig. 2). Ground base test (one-g) samples were of necessity processed in a sessile configuration and, as shown in Fig. 3, demonstrated an asymmetry partly resulting from the gravitational body force, mg. Another contribution to this asymmetry is the increasing internal pressure of the liquid at increasing depth as a result of the gravitationally dependent hydrostatic pressure head. None of the ground base processed samples, however, exhibited macroscopic distortions (Ref. 2) comparable to that shown in Fig. 1.

It has been proposed that the macroscopic distortion (Ref. 2) demonstrated by some of the Skylab II M553 processed materials was due to cavitative reactions that occurred in low-g because of the appreciable reduction in the internal pressure of the metallic liquids. Since only some of the Skylab II processed samples had voids, one possible explanation is that cavitation is composition dependent. Other explanations include dependence on thermal history, geometry, or type of metallurgical phase reaction. All these possibilities are examined further.

INTERNAL PRESSURE OF LIQUIDS

The total local pressure (P_t) within a column or drop of liquid is equal to the summation of the hydrostatic pressure (P_h), the surface tension pressure (P_γ), and the environmental pressure (P_e) as given by:

$$P_t = P_h + P_\gamma + P_e \qquad (1)$$

ORIGINAL PAGE IS OF POOR QUALITY

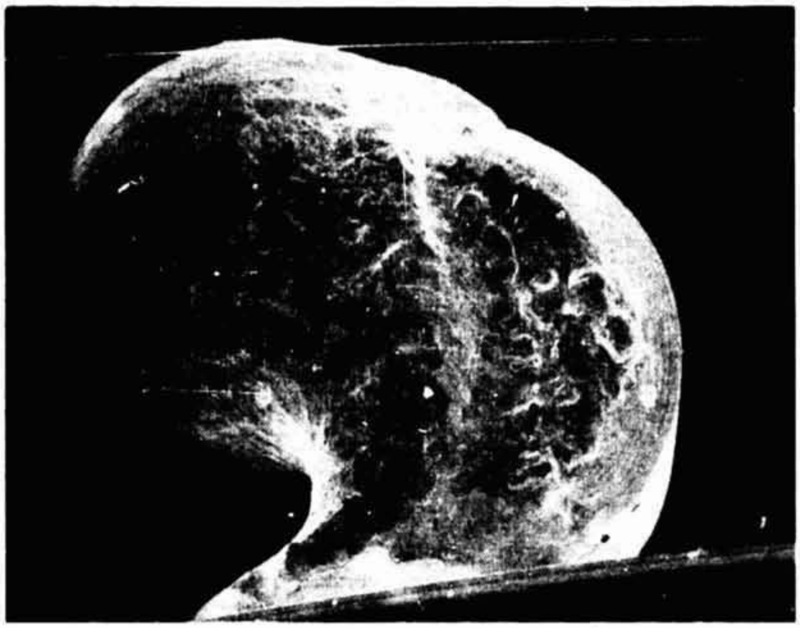

Fig. 1 Macrophotograph of Skylab II, M553, Sample 1.13, Ni-1 Ag (15x)

Fig. 2 Macrophotograph of Skylab II, M553, Sample 1.5, Ni-12Sn (15x)

If only vacuum processing in low-g is considered, then the environmental pressure term is insignificant relative to the other terms, and the total local pressure (P_{tv}) at any point in a liquid is:

$$P_{tv} = P_h + P_\gamma \tag{2}$$

(In this treatment and what follows we do not consider the effect of any externally applied fields.)

The local hydrostatic pressure (P_h) in a liquid is given by:

$$P_h = \delta g h \tag{3}$$

where

δ is the specific weight of the liquid, g is the gravity level, and h is the height of liquid above the point of interest.

For a spherical geometry, P_γ is directly proportional to the surface tension (γ) of the liquid at the temperature of interest and inversely proportional to the radius of the sphere (R_o) as shown by

$$P_\gamma = \frac{2\gamma}{R_o} \tag{4}$$

Thus, the total internal pressure of the drop is given by:

$$P_{tv} = P_h + P_\gamma = \delta g h + \frac{2\gamma}{R_o} \tag{5}$$

Since the geometry of the M553 specimens was intended to be spherical, or a sessile configuration which is ideally a truncated sphere, we calculate P_{tv} for a spherical drop of radius R_o. The geometrical considerations are shown in Fig. 4.

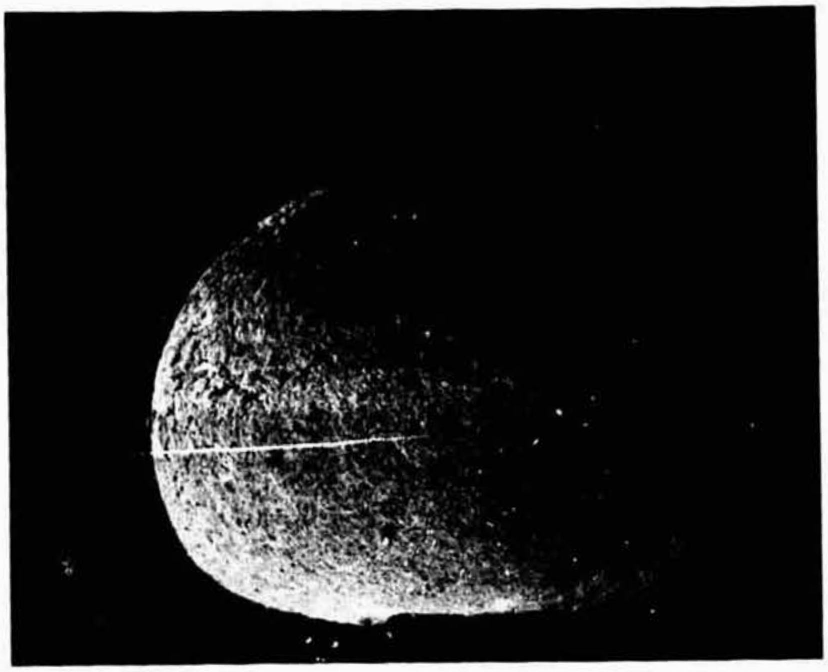

Fig. 3 Ground Base Processed Sample, Ni-12Sn (15x)

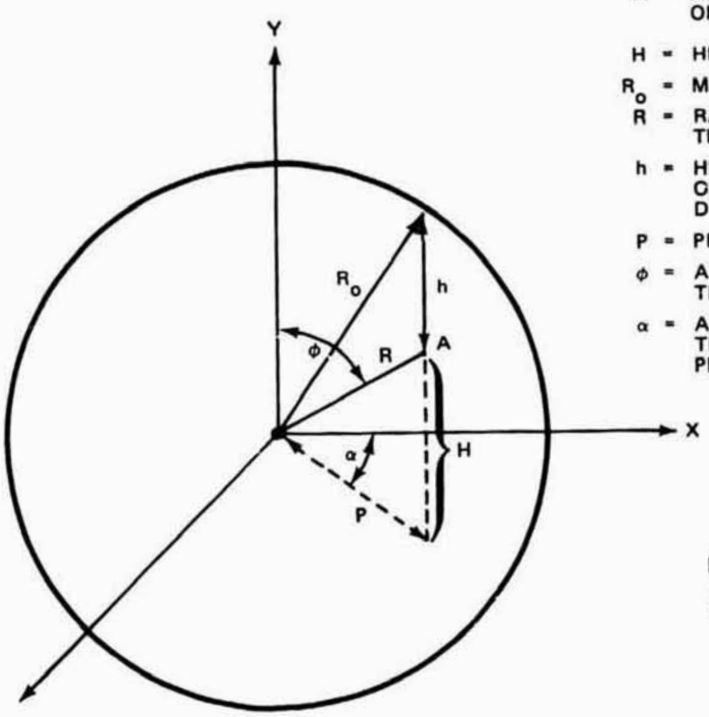

A = ARBITARY POINT OF INTEREST

H = HEIGHT ABOVE X, Z PLANE

R_o = MAXIMUM RADIUS OF THE SPHERE

R = RADIUS TO POINT OF INTEREST FROM THE ORIGIN

h = HEIGHT OF LIQUID ABOVE THE POINT OF INTEREST, IN THE GRAVITATIONAL DIRECTION

P = PROJECTION OF R IN THE X, Z PLANE

ϕ = ANGLE BETWEEN THE Y AXIS AND THE RADIUS R

α = ANGLE BETWEEN THE X AXIS AND THE PROJECTION OF R IN THE X, Z PLANE

NOTE: h IS INDEPENDENT OF α BECAUSE OF THE ROTATIONAL SYMMETRY ABOUT THE Y AXIS. GRAVITY IS IN THE NEGATIVE Y DIRECTION.

Fig. 4 Arbitrary Point of Interest, A, Shown in a Spherical Drop of Radius R_o.

To determine the change in internal pressure of the drop with g, it is necessary to consider how both P_h and P_γ vary with drop size and g. For the hydrostatic term, h will vary with location within the spherical volume, as shown in Fig. 4. This variation is derived in the Appendix and is given by:

$$h = \left[R_o^2 - R^2 \cos^2 (90-\phi)\right]^{\frac{1}{2}} - R \sin (90-\phi) \tag{6}$$

where:

R_o = Maximum Radius of Sphere

R = Radius to Point of Interest

ϕ = Angle between the Y axis (-g direction) and R

Consequently, P_h is a complex term which varies within the drop.

Pressure head distributions across spheres are shown in Fig. 5 for both the minimal wetting ($\theta = 90^\circ$) and maximum nonwetting ($\theta = 180^\circ$) conditions. The pressure head remains quite high throughout the bulk of the drop at these high contact angles and diminishes to low levels only close to the surface of the sphere. This fact and the selection of nonwetting sessile pedestals serve to support the subsequent usage of a hydrostatic head equal to twice the sphere radius, R_o. This results in a maximum value of the hydrostatic pressure term being utilized throughout. In a typical low-g environment, $g = 10^{-4}$g earth, and the hydrostatic term becomes vanishingly small.

This variation of the terms of the summation is shown in Fig. 6 for a range of surface tension (γ), specific weight (δ), and radius (R_o). These values are representative of almost the entire spectrum of metallic and organic liquids. The sample sizes are consistent with space processing capabilities.

Table 1 (from Ref. 3) gives values of δ and γ for some typical materials, which are of potential importance to space processing. Considerable scatter exists in published surface tension values, perhaps because low impurity levels can appreciably lower the surface tension of pure elements.

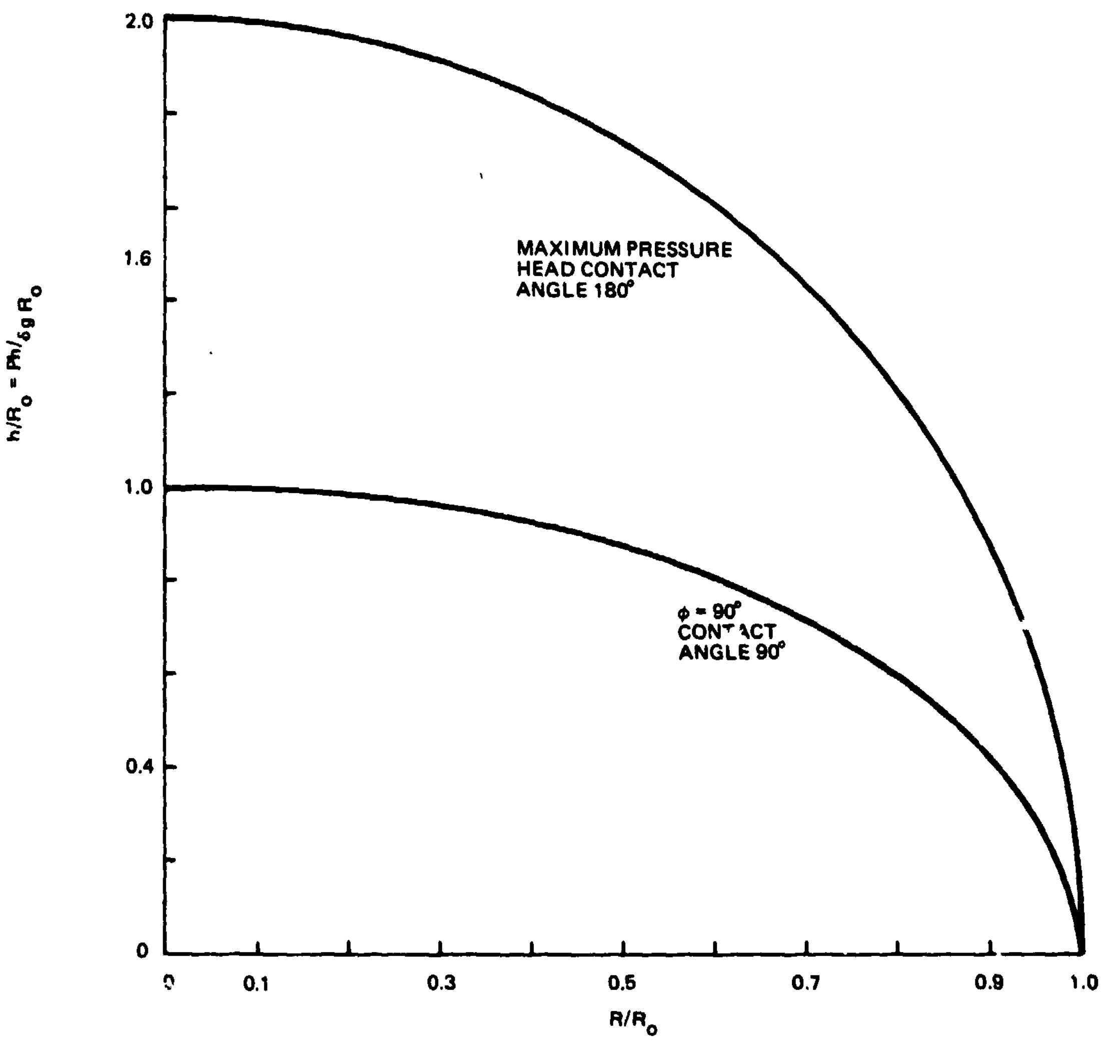

Fig. 5 Variation of Normalized Pressure Head Within Spherical Droplet of Radius R_o

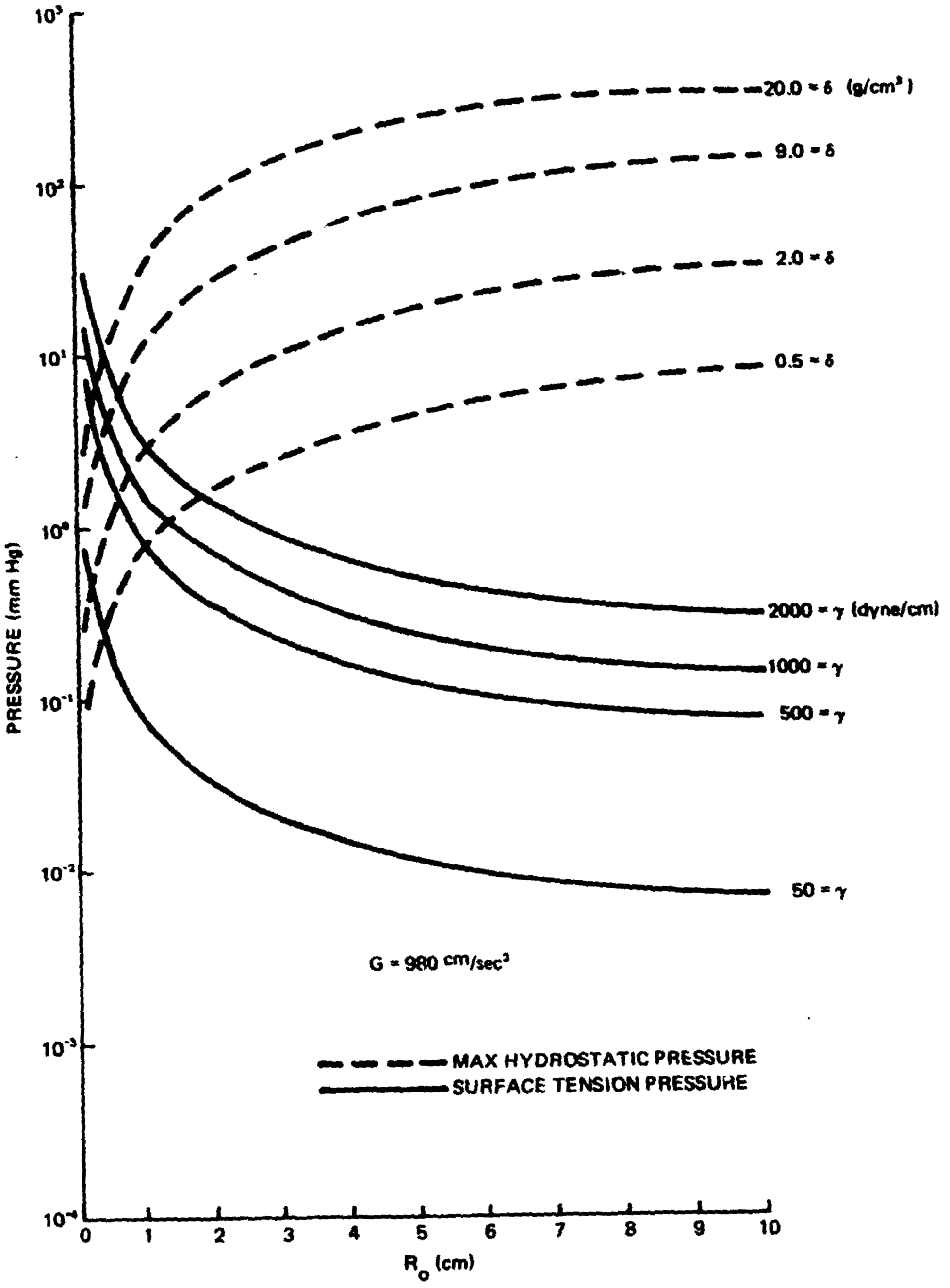

Fig. 6 Variation of Maximum Hydrostatic Pressure and Surface Tension Pressure as a Function of Specimen Radius (R_o), Density (δ), and Surface Tension (γ)

TABLE 1 SELECTED VALUES OF SPECIFIC WEIGHT (δ) AND SURFACE TENSION (γ) FROM REF. 3

Material	Specific Weight (δ) g/cm^3	Surface Tension (δ) dyne/cm*
Ni	8.90	2100
Fe	7.87	1880
Cu	8.96	1300
Si	2.5	720
Ge	5.6	650
GaAs	5.7	530
InSb	6.7	440
Al	2.70	500
Na	0.81	202
H_2O	1.0	73
Benzene	0.9	29
Napthalene	0.98	29

* At the melting point

Figure 6 shows that surface tension pressure decreases with size, whereas the maximum hydrostatic pressure increases. Selecting a specific weight of 9.0 g/cm^3 as representative of the materials processed in the M553 experiment, we see in Fig. 7 the dramatic impact of gravity level upon the hydrostatic pressure term.

Terrestrially, in one-g vacuum processing, P_h is the dominant term for all but the smallest of samples; however, as the gravity level is reduced to a realistic orbital level of 10^{-4}g, it becomes considerably smaller than the surface tension pressures of virtually all metallic liquids ($200 < \gamma < 2000 \frac{\text{dyne}}{\text{cm}}$). In Figs. 8-10 we have plotted the internal pressure as a function of specimen radius for three materials of different surface tension and specific weight. In one-g the two terms of the summation compensate for one another as the size changes; thus, the internal pressure does not vary greatly over a wide size range and is usually assumed constant in materials processing (Ref. 4). However, for vacuum processing of materials in low-g, it is reasonable to expect that the internal pressure will drop to approximately the value of the surface tension pressure at or below 10^{-4}g, and this result is an important consideration in the planning of any low-g experiments. The two to three orders of magnitude reduction in internal pressure for moderate sized samples processed in low-g will bring the total internal pressure of a drop to 10^{-2} to 10^{-1}mm Hg. Having established the pressure reduction and magnitude of internal pressure in a molten metallic drop in a vacuum in low-g, we will next consider the effects on phase reactions.

PHASE RELATIONS

A 100 to 1000-fold reduction in internal pressure has little effect on solid-liquid transitions as shown by the Clausius-Clapeyron equation:

$$dP/dT = \Delta H_f/T\Delta V_f \tag{7}$$

where

P = pressure (atm)

T = temperature (K)

ΔH_f = enthalpy of fusion (cal/g-atom)

ΔV_f = volume change of fusion (cm^3/g-atom)

For a typical metal sample, a pressure change (dP) of 1000 mm Hg would only change the melting point (dT) by 0.01K because of the small volume change (ΔV) on melting. This is clearly insignificant in all practical applications. However, the same pressure change would cause a temperature change $dT' \cong 0.1T_{vp}$ at the vaporization point (T_{vp}) of a metal because of the large ΔV associated with vaporization. For high or intermediate melting point materials this dT′ might be several hundred degrees and is obviously an appreciable consideration. Even an organic system with a boiling point of 300K might have a temperature shift in vapor-liquid equilibria of 30K.

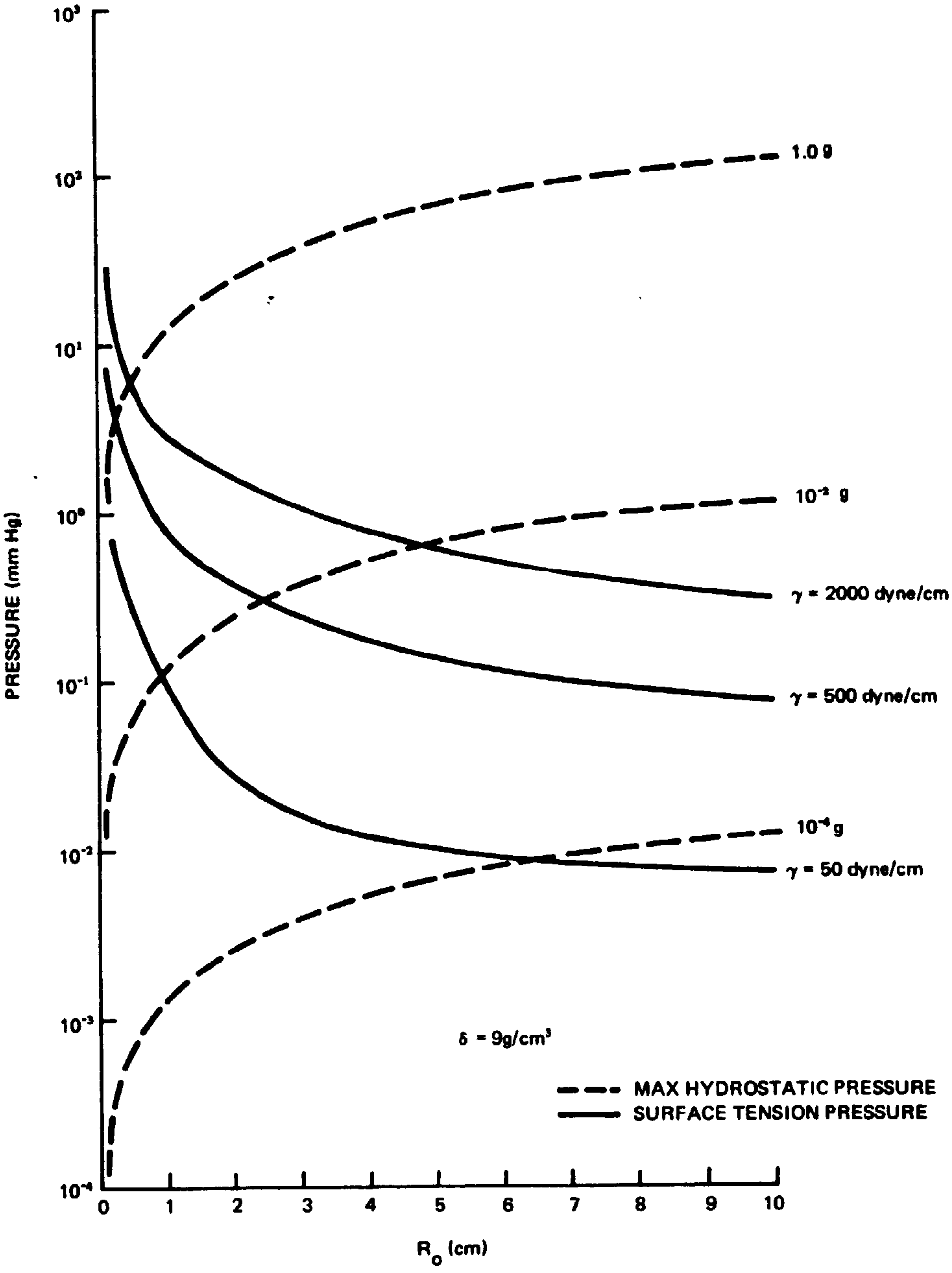

Fig. 7 Variation of Maximum Hydrostatic Pressure and Surface Tension Pressure as a Function of Specimen Radius (R_o), Surface Tension (γ), and Gravity Level (G) for a Material with a Specific Weight (δ).

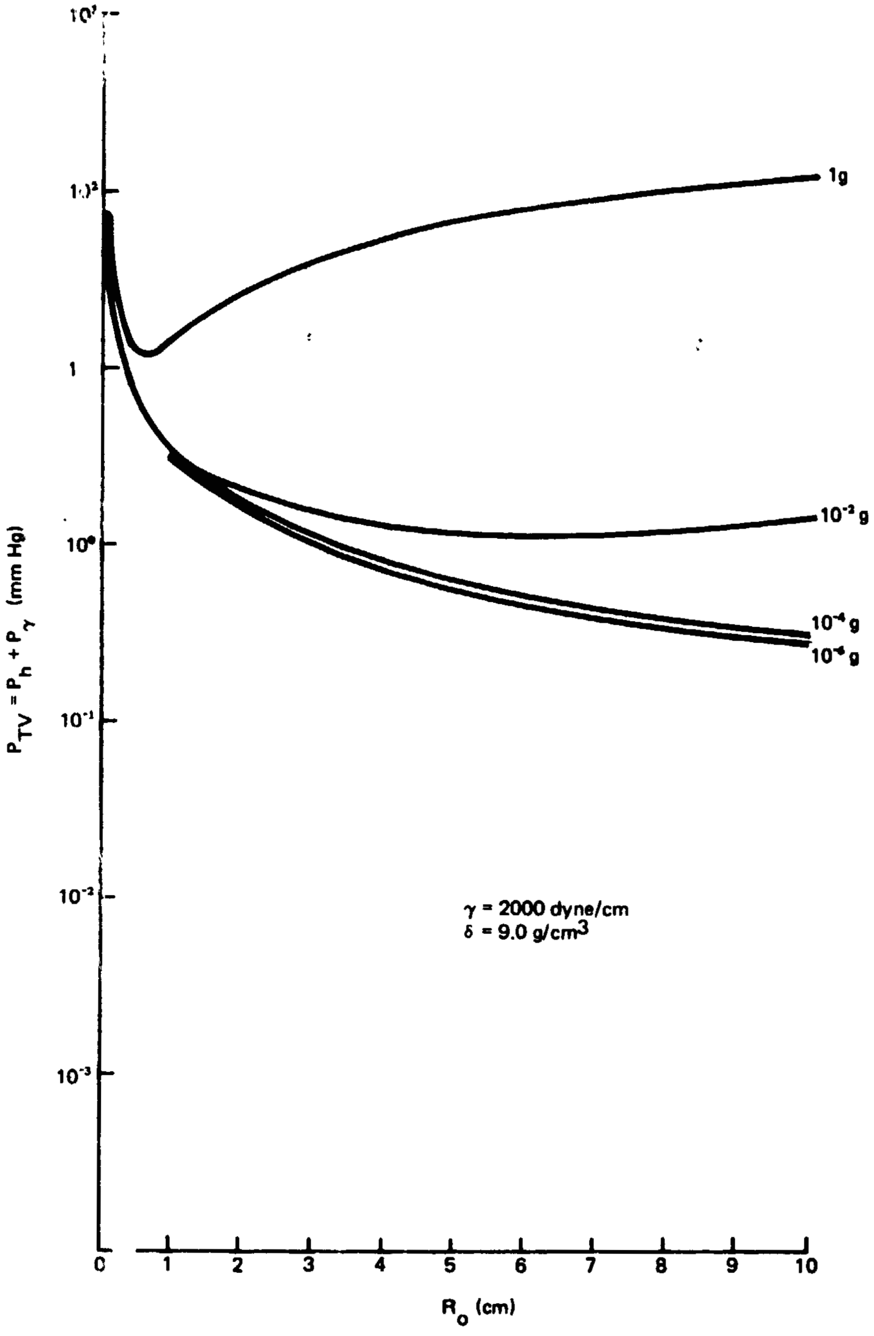

Fig. 8 Variation of Internal Pressure Summation (P_h+P_γ) as a Function of Specimen Radius (R_o) and Gravity Level (g) at Constant Specific Weight (δ) and Surface Tension (γ).

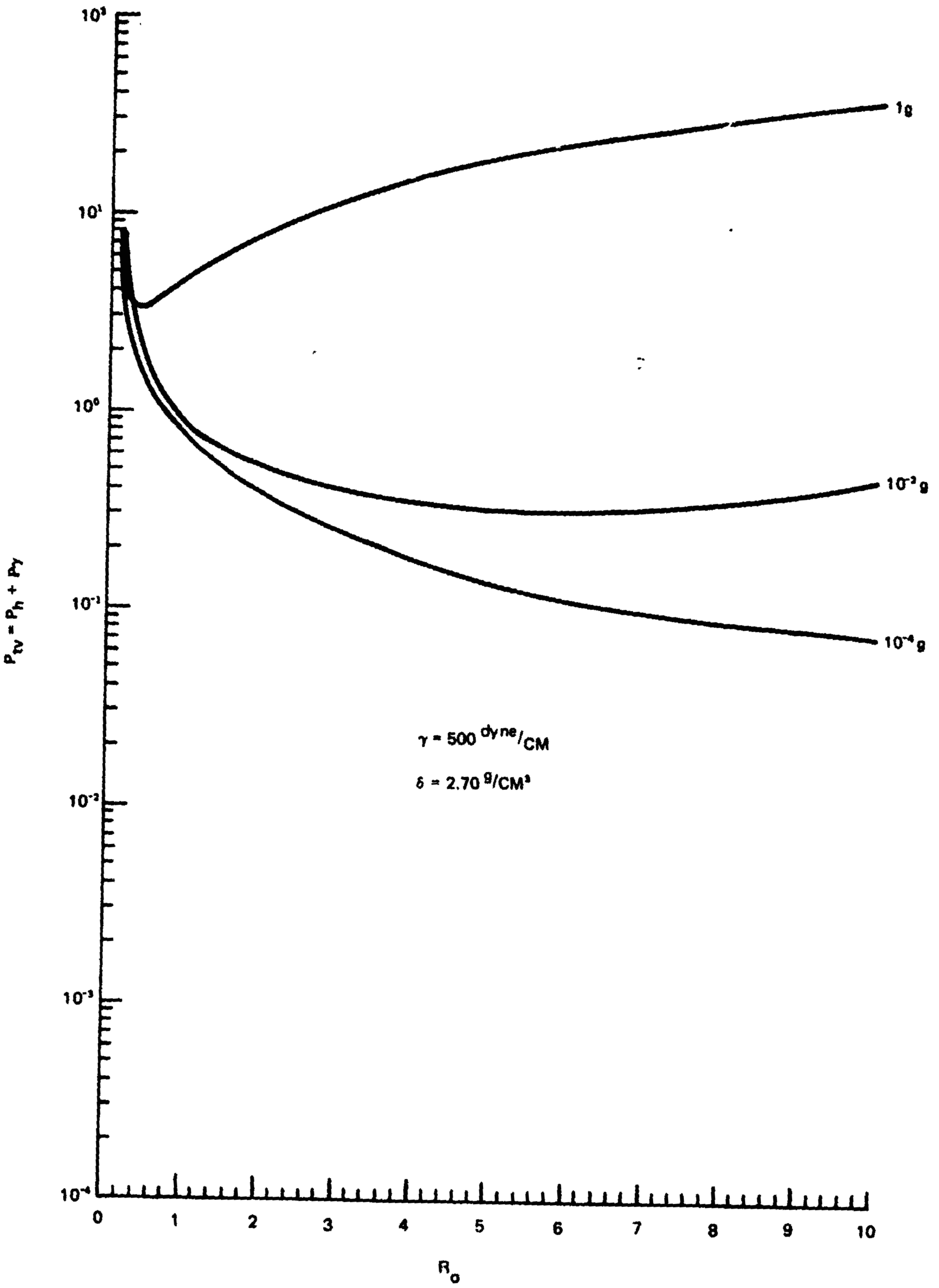

Fig. 9 Variation of Internal Pressure Summation (P_h+P_γ) as a Function of Specimen Radius (R_o) and Gravity Level (g) at Constant Specific Weight (δ) and Surface Tension (γ).

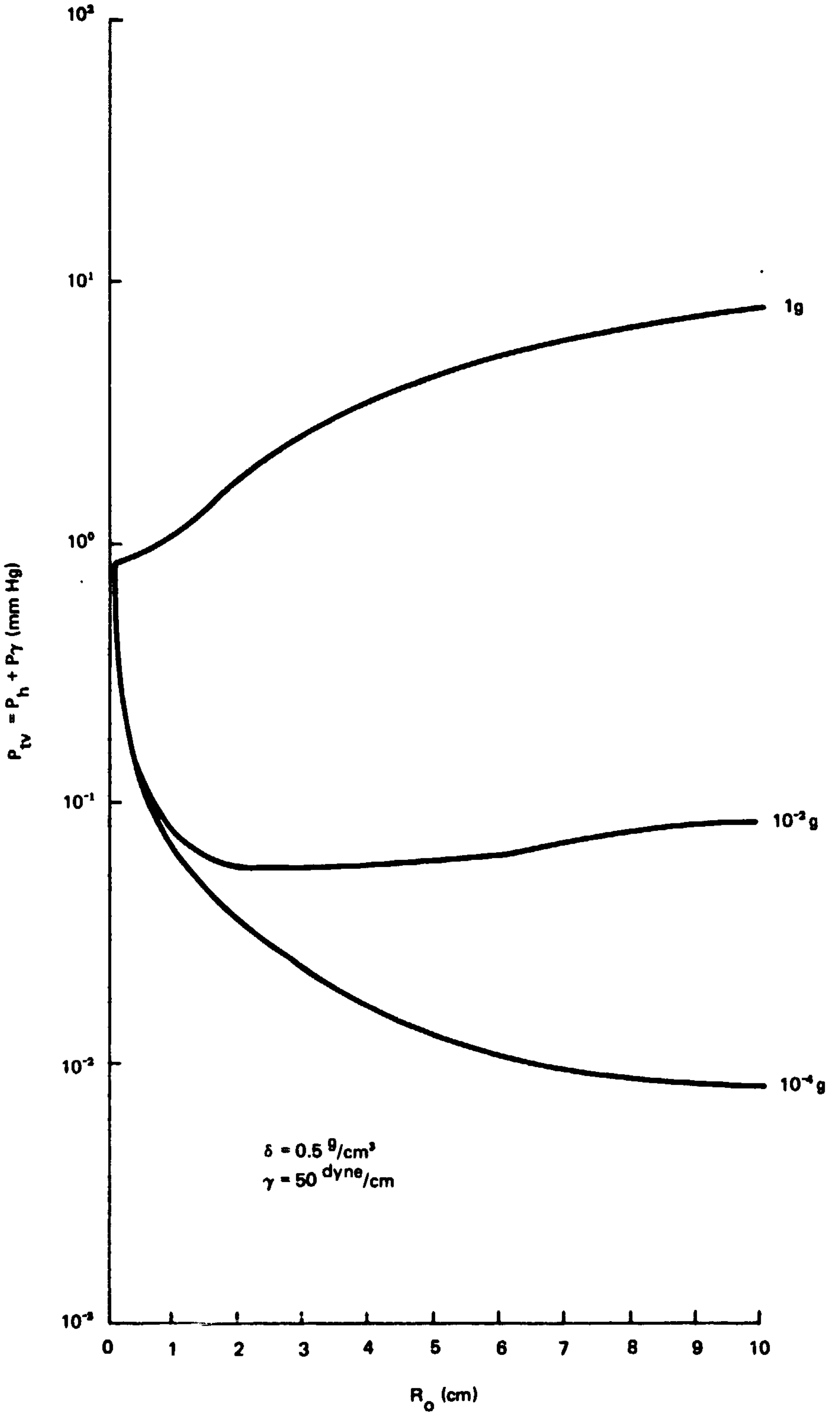

Fig. 10 Variation of Internal Pressure Summation ($P_h + P_\gamma$) as a Function of Specimen Radius (R_o) and Gravity Level (g) at Constant Specific Weight (δ) and Surface Tension (γ).

The preceding discussion strongly suggests that solid/liquid/vapor and liquid/liquid/vapor rather than liquid/solid equilibria involve substantial differences when vacuum processing materials in low-g. Although this may seem to be an added complexity, it is really of fundamental importance and a great opportunity. Terrestrially, we define solidification morphologies through control of only six solidification reactions (congruent, isomorphous, eutectic, monotectic, peritectic and syntectic). They are the only ones available to the metallurgist and involve only solid/liquid equilibria. In space we can consider controlled solid/liquid/vapor and liquid/liquid/vapor processing, which expands the number of controllable solidification reactions from 6 to 26. Twenty four are listed in Tables 2 and 3 by reaction type, the other two being congruent and isomorphous reactions. Although some of these reactions on close inspection would appear to be unlikely to occur, there is no question that the number of controllable reactions that are orbitally available to the metallurgist is substantially increased. The significance of this is that in one-g each controllable solidification reaction available to the metallurgist has proven to be both useful and of great commercial value.

If all of the previously considered phase reactions occur in absolute pressure ranges well below those that we can reasonably expect to attain in orbit (i.e., 10^{-1} to 10^{-2} mm Hg), then further detailed consideration is pointless. Clearly, the onset of solid/liquid/vapor effects will occur most readily in the vicinity of the triple points of one or more of the constituent element(s), or within alloy systems where one or more of the constituent elements has a high vapor pressure at its melting point. In metal systems the triple point temperature and melting point temperatures are effectively the same because of the nearly infinite slope of the solid/liquid curve. Thus, we must first consider which elements or congruent melting compounds have vapor pressures of 10^{-1} to 10^{-2} mm Hg or above at their melting points. Table 4 lists the vapor pressures of elements that qualify in this respect. The number of elements is clearly substantial, and the number of binary or ternary combinations involving these elements singly or in combination is virtually limitless. Space processing thus offers a substantial number of new reactions to the metallurgist in virtually a limitless number of metallic systems. We will now consider each binary reaction separately.

TABLE 2 BINARY EUTECTIC TYPE REACTIONS

1.	$L_I \rightleftharpoons \alpha + \beta$	Eutectic
2.	$L_I \rightleftharpoons \alpha + L_{II}$	Monotectic
3.	$\alpha \rightleftharpoons L_I + \beta$	
4.	$\alpha \rightleftharpoons L_I + L_{II}$	
5.	$\alpha \rightleftharpoons G + \beta$	
6.	$G \rightleftharpoons L_I + L_{II}$	
7.	$G \rightleftharpoons L_I + \alpha$	
8.	$G \rightleftharpoons \alpha + \beta$	
9.	$L_I \rightleftharpoons G + L_{II}$	
10.	$L_I \rightleftharpoons G + \alpha$	
11.	$L_I \rightleftharpoons L_{II} + L_{III}$	
12.	$\alpha \rightleftharpoons G + L_I$	

TABLE 3 BINARY PERITECTIC TYPE REACTIONS

1.	$L_I + \beta \rightleftharpoons \alpha$	Peritectic
2.	$L_I + L_{II} \rightleftharpoons \alpha$	Syntectic
3.	$L_I + L_{II} \rightleftharpoons G$	
4.	$L_I + \alpha \rightleftharpoons G$	
5.	$\alpha + \beta \rightleftharpoons G$	
6.	$G + L_{II} \rightleftharpoons L_I$	
7.	$G + \alpha \rightleftharpoons L_I$	
8.	$L_{II} + L_{III} \rightleftharpoons L_I$	
9.	$L_{II} + \alpha \rightleftharpoons L_I$	
10.	$\alpha + \beta \rightleftharpoons L_I$	
11.	$G + L_I \rightleftharpoons \alpha$	
12.	$G + \beta \rightleftharpoons \alpha$	

TABLE 4 VAPOR PRESSURES OF ELEMENTS WITH VAPOR PRESSURES GREATER THAN 10^{-1} mm Hg AT THEIR MELTING POINTS

Element	Melting Point (K)	Vapor Pressure (mm Hg)	
		Ref. 7	Ref. 8
K_2	336.35	$2.03 \cdot 10^{-1}$	-
Mg	922	2.80	3.10
Ca	1122	1.97	1.50
Sr	1041	1.91	1.61
Ba	1002	$7.59 \cdot 10^{-1}$	$3.94 \cdot 10^{-1}$
Ra	973	2.54	-
Zn	692.7	$1.49 \cdot 10^{-1}$	$1.57 \cdot 10^{-1}$
Cd	594.2	$1.15 \cdot 10^{-1}$	$1.09 \cdot 10^{-1}$
Sc	1812	$1.71 \cdot 10^{-1}$	$8.44 \cdot 10^{-2}$
Sm	1345	4.36	3.18
Eu	1090	1.12	$7.15 \cdot 10^{-1}$
Gd	1585	189	$1.56 \cdot 10^{-4}$
Yb	1097	3.06	19.76
Lu	1936	19.1	$1.11 \cdot 10^{-2}$
P_4 (wh)	317	$1.61 \cdot 10^{-1}$	-
Σ Sb	904	$1.93 \cdot 10^{-1}$	$1.56 \cdot 10^{-1}$
Σ Te	722.7	$1.79 \cdot 10^{-1}$	$1.76 \cdot 10^{-1}$
Cr	2130	7.70	3.25
Mn	1517	$9.38 \cdot 10^{-1}$	1.03
Co	1768	1.36	5.[illegible]9 $\cdot 10^{-3}$
Ni	1726	1.84	$3.10 \cdot 10^{-3}$

TABLE 4 VAPOR PRESSURES OF ELEMENTS WITH VAPOR PRESSURES GREATER THAN 10^{-1} mm Hg AT THEIR MELTING POINTS (Continued)

Element	Melting Point (K)	Vapor Pressure (mm Hg)	
		Ref. 7	Ref. 8
F_2	53.5	3.80	1.89
Cl_2	172.2	10.1	10.44
Br_2	265.9	45.0	44.61
At_2	575	373	-
Ar	83.8		516.88
Dy	1682	-	5.91×10^{-1}
Er	1795	-	3.17×10^{-1}
H	13.8	-	52.78
Ho	174.3	-	5.38×10^{-1}
I_2	386.7	-	90.82
Kr	115.8	-	548.7
N	63.1	-	93.86
O	54.4	-	1.12
Rn	202.0	-	501.60
Tm	1818	-	73.42
Xe	161.4	-	611.80
As	1092.5	-	$2.77 \cdot 10^{4}$

Elemental (Congruent)

This section not only introduces terminology and concepts but also discusses elemental reactions in low-g. Figure 11 shows the P-T (pressure-temperature) diagram for an elemental material. Since it is compositionally invariant there is no need for a third dimension (composition). For binary alloys, however, the diagrams are presented as P-T-X (pressure-temperature-composition) diagrams. For convenience, these are often shown as two-dimensional P-T projections.

The solid/liquid line in Fig. 11 has a positive slope for any element that contracts upon solidification and a negative slope for an element that expands upon solidification. In this report we assume an infinite slope for this boundary. This in no way limits any of the discussion or conclusions drawn. Since the melt temperature will be constant with pressure, however, it does simplify the notation.

Isothermal and Isobaric Effects

If the total internal pressure (P_1) within a unary liquid A in one-g is not substantially greater than its vapor pressure at the triple point (P_{QA}), then the reduction in internal pressure (ΔP_a) associated with going from one-g to low-g may cause the liquid to cavitate. This pressure change is shown in Fig. 11. If the liquid/vapor equilibrium line is not crossed owing to an insufficient reduction in internal pressure on going to low-g, there is still a possibility that cavitation can occur. In this case the reduction in internal pressure (ΔP_b) has reduced the temperature increase before the onset of cavitation from ΔT_a to ΔT_b. This reduced tolerance to overheating in the low-g environment must be taken into consideration during processing of all materials in the weightless state, regardless of reaction type. More complex phase reactions behave in the same fashion and are treated below and will be treated in the next memorandum.

Isomorphous

If an isomorphous solid alloy is completely homogenized, then its behavior on melting will be no different than the unary system considered previously.

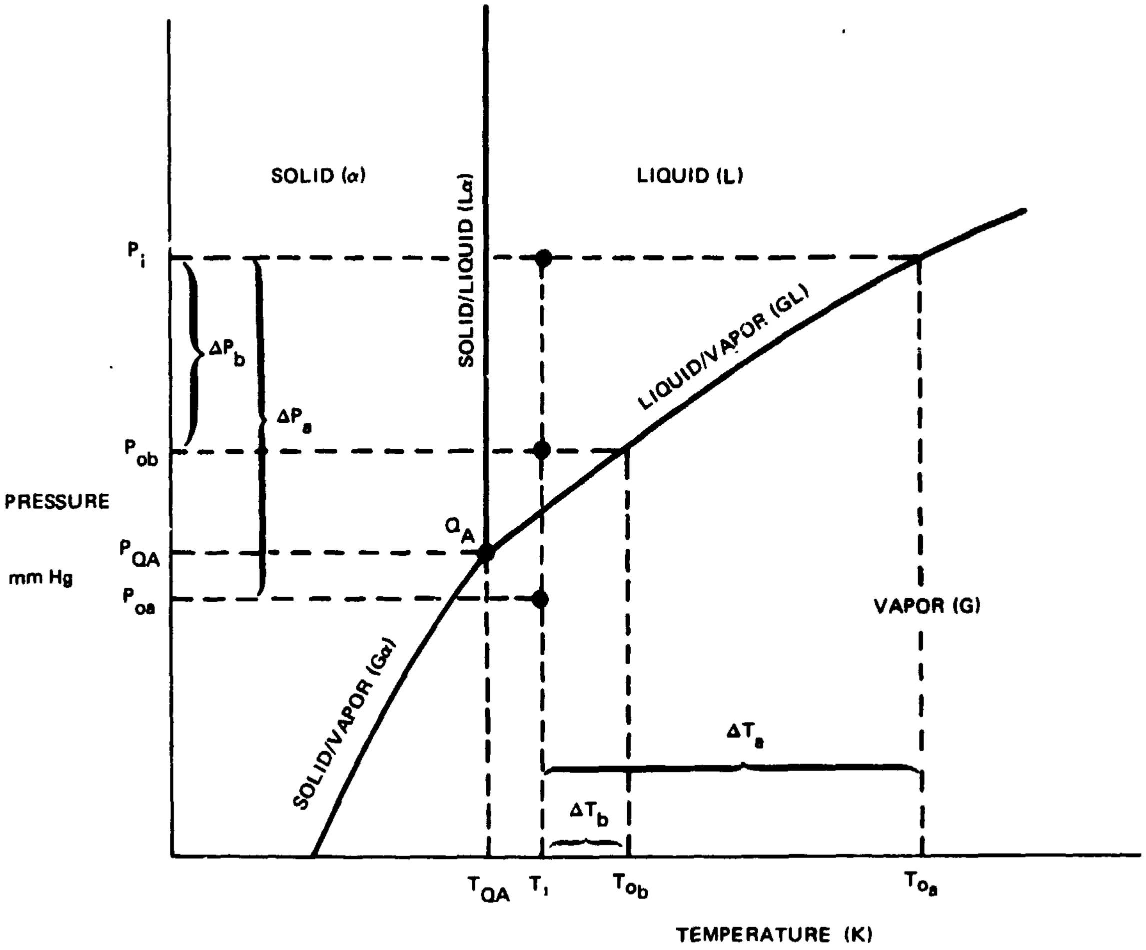

Fig. 11 Pressure-Temperature Diagram for Unary System

Material not homogenized because of prior processing will have a range of liquidus and solidus curves because of the nonuniform composition. These must be treated in a different manner than homogenized isomorphous alloys.

Nonhomogeneous Isomorphous Solids ("Cored" Structures)

Cored microstructures are compositionally nonhomogeneous. In the following case it is assumed that the solute (B) lowers the alloy melting point. If the internal pressure of the high solute content material is not substantially above the triple point of the solute-rich liquid, this liquid might cavitate immediately on melting in low-g or during the superheating necessary to melt the remaining lower solute content solid. A P-T projection of this type is shown in Fig. 12 for an isomorphous alloy with solute-poor composition A and solute-rich composition B. Internal pressure at one-g (P_1) and low-g (P_o), respectively, are shown. At P_1, the low melting constituent melts at T_{mB}. However, to melt the A component, a temperature of T_{mA} must be reached. This poses no problem in one-g at P_1 since the entire system can be superheated ΔT_1 above T_{mA} before cavitation occurs. Cavitation is unlikely because liquid mixing will occur well before that temperature is reached, and this degree of superheat will be experimentally unnecessary.

At P_o in low-g, the same sequence will not occur. The B component will melt at T_{mB}, and this liquid will cavitate during heating on crossing the GL_B line ΔT_o below the melting point of A. If the A component were distributed as a continuous array or network, then the sample might well "spit" or break up as the GL_B line is crossed. This will occur without the melting of A or the uniform mixing of the A and B liquids. From a foundry standpoint this is unacceptable. Additional considerations relate directly to the physical properties of the alloys in question and the resulting phase relations that these properties impose in the pressure and thermal orbital environment.

Figure 13 illustrates the three types of P-T projections that categorize all isomorphous binary alloy systems. These may be described in mathematical notation:

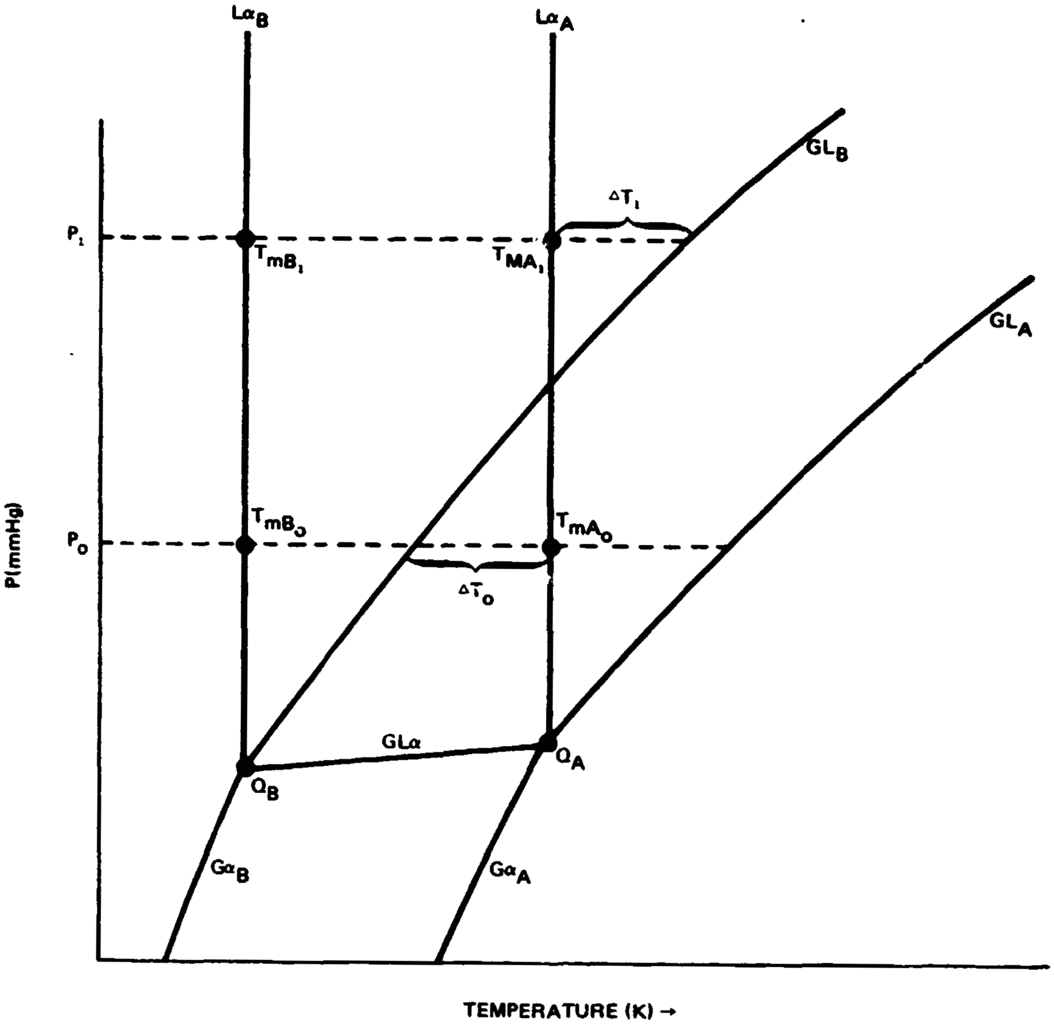

Fig. 12 Pressure-Temperature Diagram for Isomorphous Solid

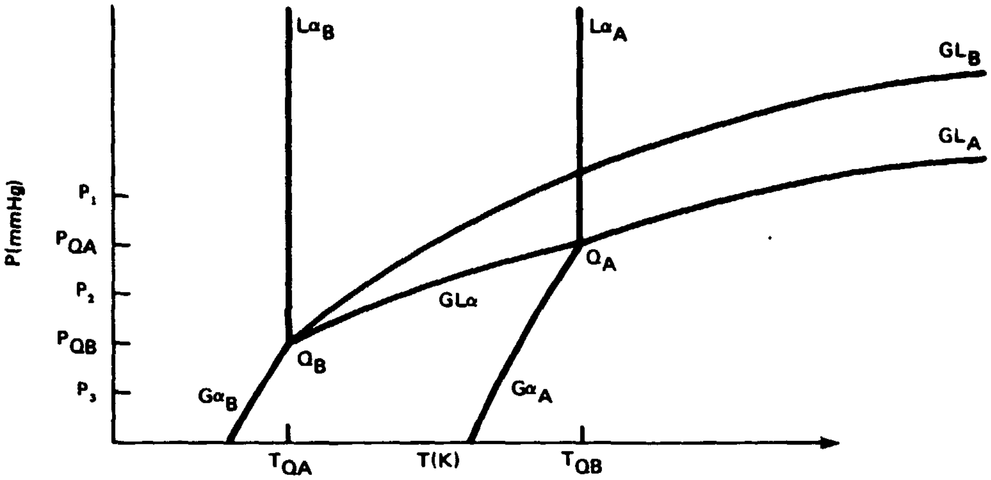

a) Case A, Isomorphous System

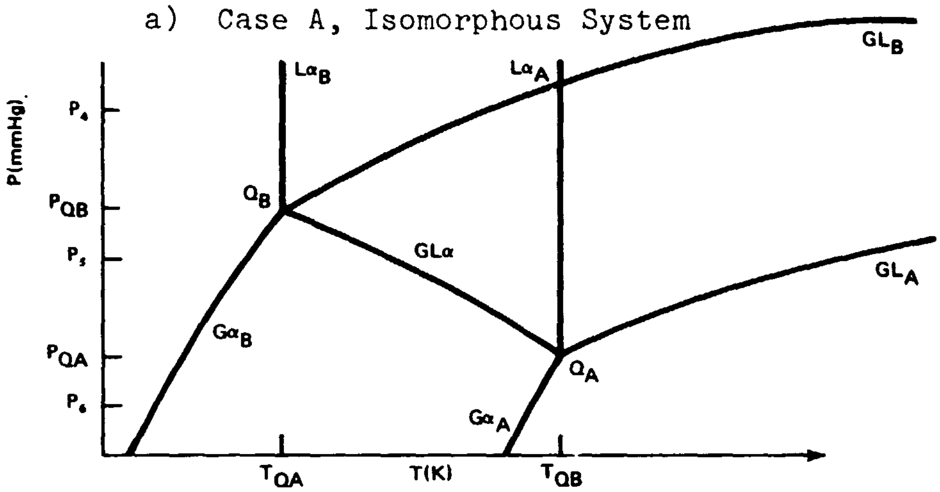

b) Case B, Isomorphous System

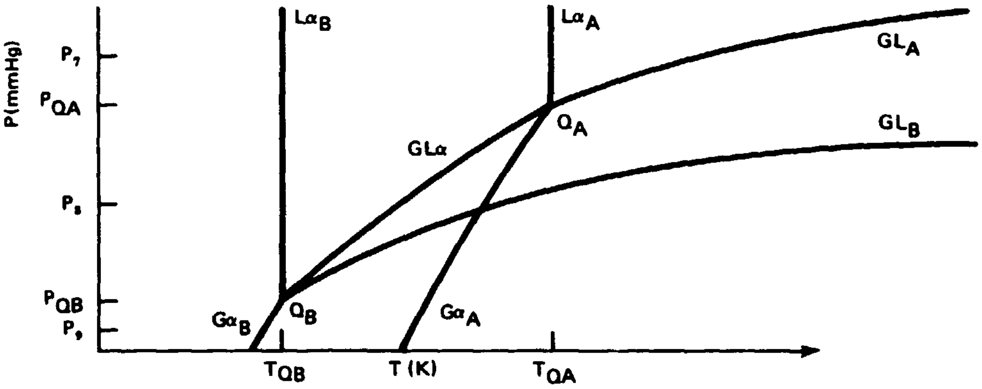

c) Case C, Isomorphous System

Fig. 13 Isomorphous Pressure-Temperature Projections (P-T) for Binary Systems A-B.

Case A - $T_Q > T_Q$, $P_Q > P_Q$, $P_Q < P_{GL_A}$ at T_Q

Case B - $T_Q > T_Q$, $P_Q < P_Q$, $P_Q < P_{GL_A}$ at T_Q

Case C - $T_Q > T_Q$, $P_Q > P_Q$, $P_Q > P_{GL_A}$ at T_Q

Consideration of the isobars P_1 to P_9 in Fig. 13 is sufficient to categorize all reaction possibilities within isomorphous systems. As indicated previously, the behavior of material on melting depends on the initial compositional homogeneity or lack thereof. Assuming the alloy to be initially homogeneous, we may treat it as an elemental system on melting and see that considerations described in the Elemental (Congruent) section apply directly. If the binary alloy is inhomogeneous, the general discussion presented in the Nonhomogeneous Isomorphous Solids ("Cored Structures") section is applicable. Reactions of specific interest to low-g processing will be presented now.

Similar temperature-composition diagrams (T-X) are generated from all three P-T diagrams at isobars P_3, P_6, and P_9. This can easily be seen by considering the sequence of phase reactions on going isobarically from high to low temperature. These involve only a solid/vapor envelope and will not be discussed further.

Isobaric sections at P_1, P_4 and P_7 will generate T-X phase diagrams, which consist of a solid/liquid envelope with an independent liquid/vapor envelope at higher temperatures. Both envelopes demonstrate total solid solubility. As the pressure is lowered from P_1, P_4, or P_7, the vapor/liquid envelope approaches the solid/liquid envelope until at and below the triple point of the element with the higher vapor pressure they intersect and the solid/liquid and liquid/vapor two phase reactions are superseded by solid/liquid/vapor three phase equilibria. These reactions occur only over pressure ranges between the triple points of the two elements or, in the case of a cored microstructure, the triple points of the maximum and minimum solute content material. This is represented in Fig. 13 by pressures P_2, P_5, and P_8.

The application of this consideration to real metallurgical systems depends on the internal pressure, composition, and geometry of the materials under investigation, but the elements listed in Table 4 will induce reactions of this type when present in a binary isomorphous alloy being processed in the orbital environment.

One of the interesting reactions in Fig. 13 is the isobaric section P_5. For this case, we have plotted the temperature-composition (T-X) diagram in Fig. 14. It is unique because cavitation can occur on cooling. Under these conditions, a solid will decompose to a stable liquid on heating, but on cooling the liquid might decompose by the following reaction:

$$L \xrightarrow[\text{cooling}]{} \alpha + G \qquad (8)$$

This reaction is limited to Case B: $T_{QB} > T_{QA}$, $P_{QB} < P_{QA}$ $P_{QB} < P_{GL_A}$ at T_{QB}.

Summarizing this section on cored microstructures, cavitation may be a problem on melting either because of a reduced tolerance to superheat brought about by lowered internal pressures or because P_{tv} of the system falls between the triple points of the binary parent species. In the latter situation, it is possible that an apparently stable liquid will cavitate (Eq. 8) on cooling, but this only would occur in systems meeting the specific compositional, pressure, and temperature conditions described by the isobaric section P_5, within a system described as Case B, and illustrated as the T-X diagram in Fig. 15.

Monotectic

A monotectic reaction as shown in Table 2 is written as:

$$L_I \leftrightharpoons \alpha + L_{II} \qquad (9)$$

A representative T-X isobaric phase diagram is shown in Fig. 15a. This diagram differs from the previous isomorphous system in that a region of liquid/liquid immiscibility and an invariant three phase α L_I L_{II} line have been superimposed in the isobaric section on the solid/liquid envelope. A monotectic reaction is generally accompanied by solid state immiscibility. The presence of a second

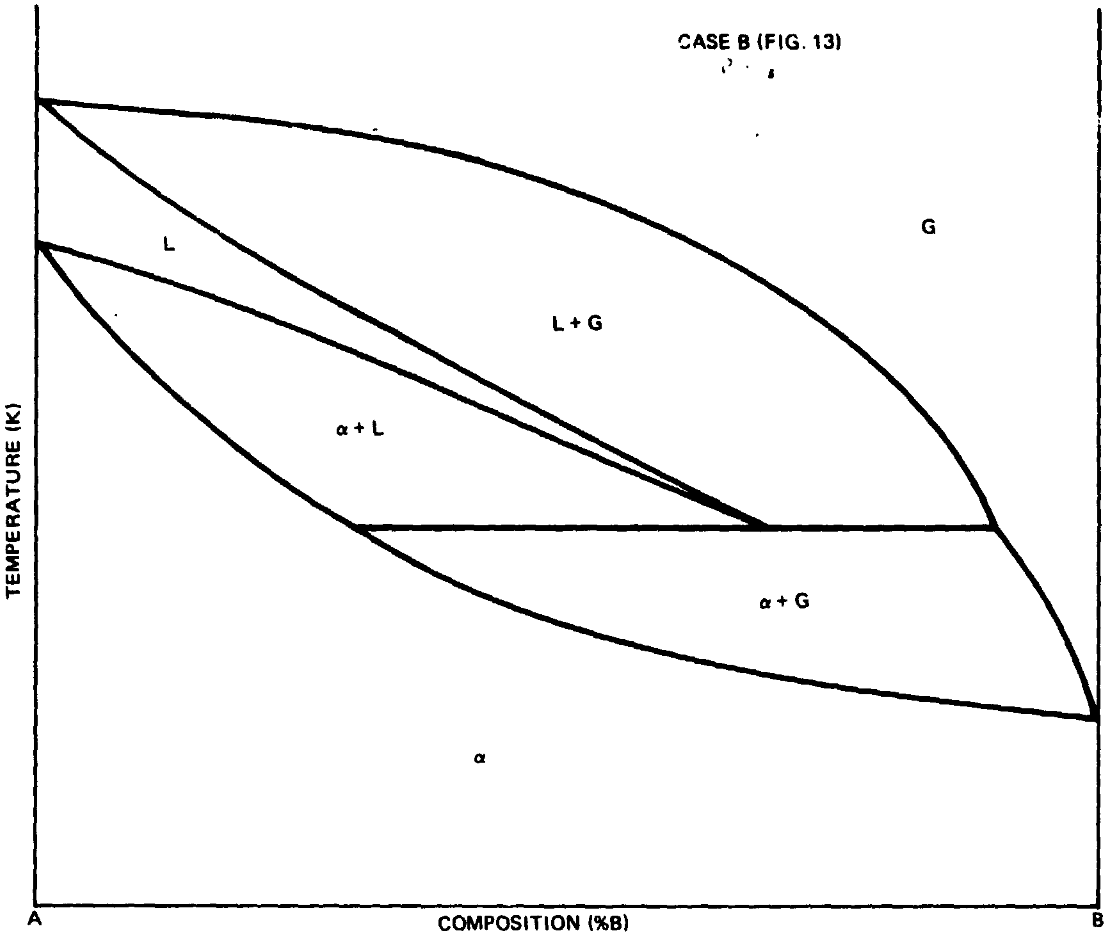

Fig. 14 Temperature-Composition Diagram of the Isobaric Section Taken from Fig. 13 Case B at Pressure P_5

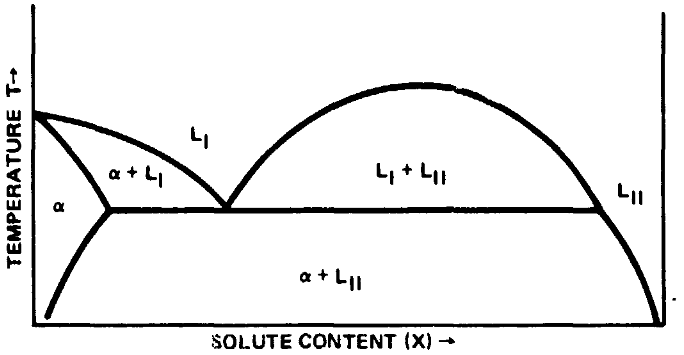

a) Temperature-Composition Diagram Showing Only a Monotectic Reaction $(L_I \rightleftharpoons \alpha + L_{II})$

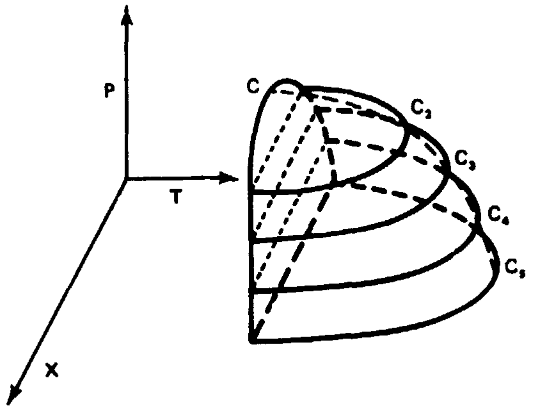

b) P-T-X View of Immiscible Region (Note Rotation of Coordinates)

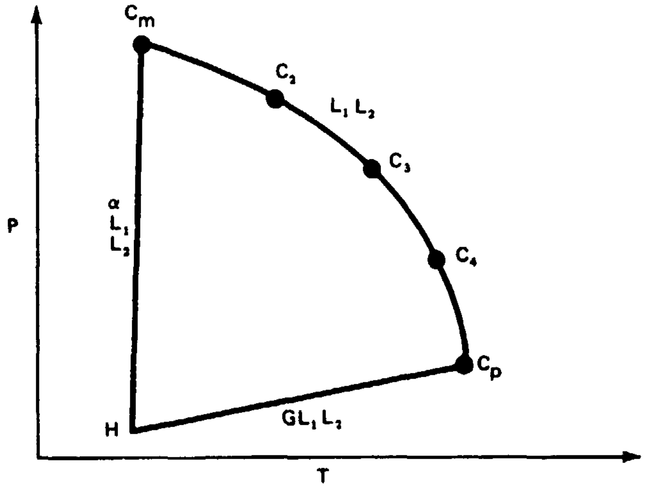

c) P-T Projection of Immiscible Region with Corresponding Critical Points (c) and Quadruple Point (H)

Fig. 15 View of Liquid-Liquid Immiscible Region in Differing Coordinate Systems solid phase, however, adds considerable complexity to the construction of P-T diagrams; therefore, the monotectic reaction is introduced here in an isomorphous solid system. Solid state immiscibility will be treated in Part 2.

The P-T projections for all isomorphous alloys may be described by the following:

Case A - $T_{QA} > T_{QB}$, $P_{QA} > P_{QB}$, $P_{QA} < P_{GL_B}$ at T_{QA}

Case B - $T_{QA} > T_{QB}$, $P_{QA} < P_{QB}$, $P_{QA} < P_{GL_B}$ at T_{QA}

Case C - $T_{QA} > T_{QB}$, $P_{QA} > P_{QB}$, $P_{QA} > P_{GL_B}$ at T_{QA}

We must now superimpose the added complexity of the region of liquid/liquid immiscibility (Fig. 15b) on any of the $GL\alpha$ three phase equilibrium lines of Fig. 13. This region projects as a "sail" and meets the $GL\alpha$ line at a four phase equilibrium point H called the quadruple point (Fig. 15c). The location of the quadruple point and the pressure and temperature extent of the sail vary with each system considered. Figure 16 illustrates the superposition of the monotectic sail on the Case B isomorphous conditions and the three possible relative locations of the quadruple point. We have previously shown that in isomorphous systems it is the Case B condition that yields unique low-g results, and so this condition is treated in detail. It is clear, too, that the critical points C_m and C_p can assume different positions relative to P_{QB}; however, this will be treated in the text and will not be separately illustrated.

Locations of isobaric sections that yield singular phase reactions are indicated as P_{10}, P_{11}, P_{12}, and P_{13}. Other isobaric sections give the same results as the isomorphous cases or a simple monotectic reaction which involves little or no change from Fig. 15a.

The analyses presented in the Isothermal and Isobaric Effects and the Nonhomogeneous Isomorphous Solids sections are pertinent to these systems for isobaric sections not in the region of the monotectic sail; however, in the vicinity of the immiscible projection there are a variety of new phase reactions to consider.

For all pressures down to the critical point C_p which marks the lower extremity of the $L_I\ L_{II}$ critical curve, and below C_p to P_{QB} if $P_{QB} < P_{Cp}$ the only gaseous considerations are the ones treated in the sections cited above (i.e., the crossing of GL_{II} at a temperature below the melting point T_{QA} of the solute-poor component). Below this pressure three phase equilibria must be considered involving solid, liquids, and vapor (α, L_I, L_{II}, and G). Cavitation must be considered on heating without superheat ($< T_{QA}$) below the pressure P_{QA} if $P_{QB} > P_{Cp}$ and below P_c if $P_c > P_{QB}$. For Case B, most of these reactions will be between the triple points of components A and B. This is the same consideration that is presented in the Isothermal and Isobaric Effects section. If $P_{Cp} > P_{QB}$ and if $P_{QB} > P_{Cp}$, the GL line is replaced by $GL_I\ L_{II}$ due to the liquid/liquid immiscibility.

Between the triple points of the two components, the isobaric T-X diagrams indicate the distinct possibility of cavitation occurring on cooling from a stable liquid, as well as on heating. These singular possibilities are shown in Fig. 16 as P_{10}, P_{11}, P_{12}, and P_{13}. At P_{10}, ($P_{10} < P_{QB} < P_{Cp}$) L_{II} decomposes to α plus G:

$$L_{II} \leftrightarrows \alpha + G \tag{10}$$

and at P_{11} ($P_{11} < P_H$), L_I decomposes to the same products :

$$L_I \leftrightarrows \alpha + G \tag{11}$$

These reactions are shown in Figs. 17a and 17b, respectively.

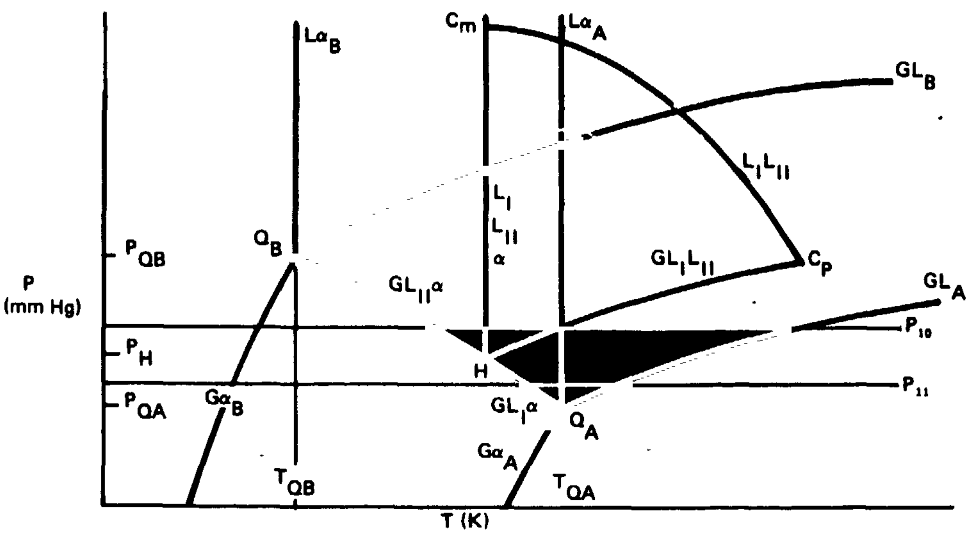

a) Case B-Monotectic System with Quadruple Point Between Triple Points

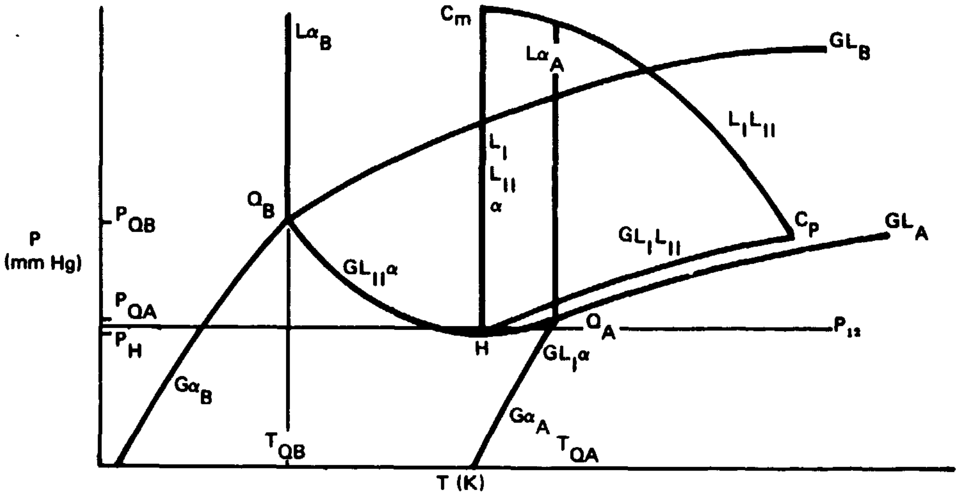

b) Case B-Monotectic System with Quadruple Point Below Triple Points

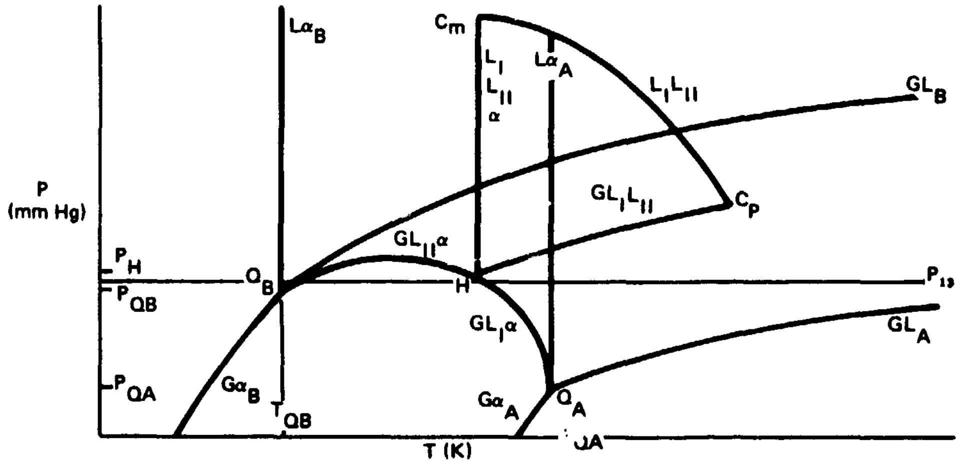

c) Case B-Monotectic System with Quadruple Point Above Triple Points

Fig. 16 Monotectic Pressure-Temperature Projections (P-T) for Monotectic Systems (A-B) of the Case B Type

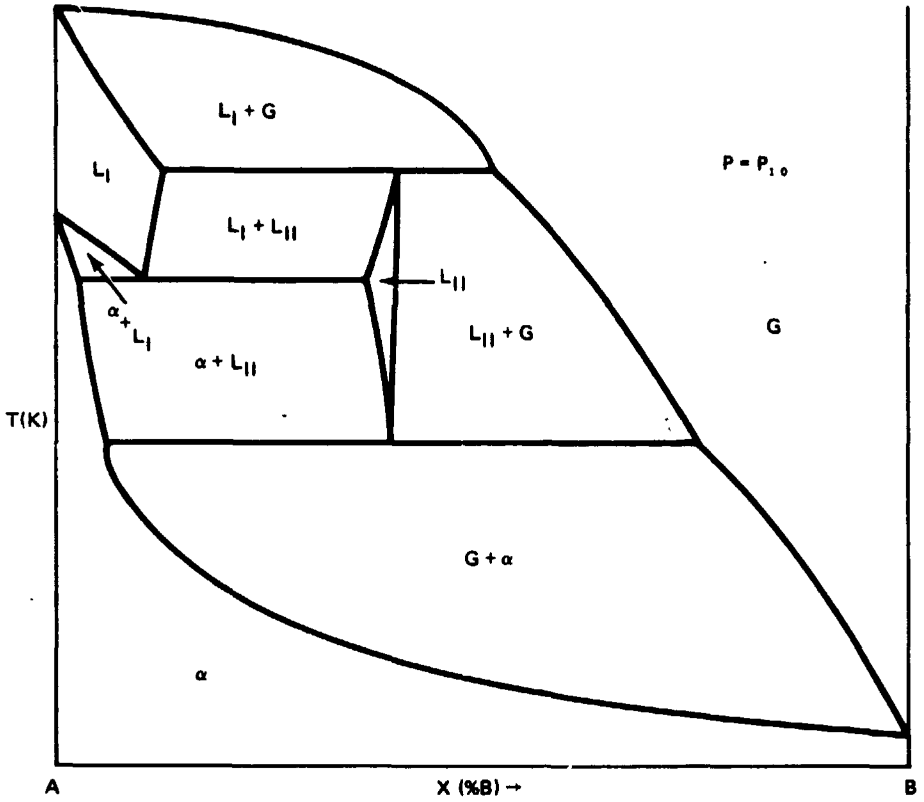

(a) T-X Diagram at P_{10} of Fig. 16a

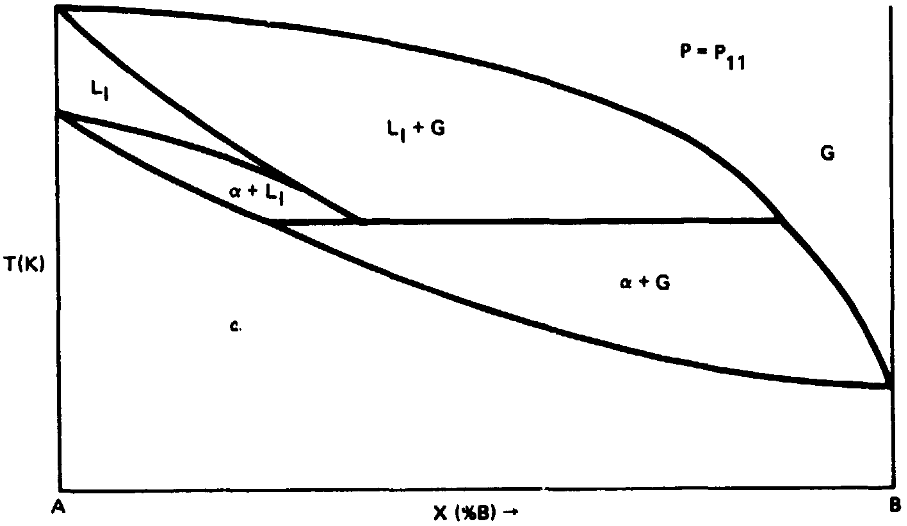

(b) T-X Diagram at P_{11} of Fig. 16a

Fig. 17 Isobaric Sections Involving Cavitative Reactions on Cooling (from Fig. 16a)

For Fig. 16b at P_{12} ($P_{QA} > P_{12} > P_H$) a complex T-X diagram results shown in Fig. 18a. On cooling, L_{II} decomposes to α plus G (Eq. 10), which is analogous to the cavitative reaction at P_{10} shown in Fig. 17a. In other pressure ranges the results are entirely consistent with discussions in the two sections cited.

A unique result occurs in the isobaric phase diagram at P_{13} ($P_H > P_{13} > P_{QB}$) in Fig. 16c, as shown in Fig. 18b. Here, L_I decomposes to α plus G (Eq. 11), which then decomposes to a secondary liquid (L_{II}), which solidifies as α (Eq. 12):

$$\alpha + G \rightleftharpoons L_{II} \tag{12}$$

This result is similar to a cavitative bubble collapsing after its formation. The significance of such a reaction is that even if the bubbles entirely disappeared (that is, if they created no macroscopic distortion of the sample) they would have disturbed the heat transfer across the sample during a portion of the processing and on collapse would likely cause high pressure pulses.

Monotectic equivalents to the isomorphous Cases A and C are shown in Figs. 19a and b, respectively. Cavitative reactions occur in these cases only under the special conditions of 'flexing' of the GLα line in pressure space. Since our main interest is in determining new solidification structures or morphologies resulting from cavitation, these will be treated, only after the generalized behavior is summarized on the basis of the Element (Congruent) and Isomorphous sections and the detailed treatment is summarized on the basis of Case B of the Isomorphous section.

Above the maximum critical points (C_m) isobaric sections result in T-X diagrams that are isomorphous sections with normal solid/liquid and gas/liquid envelopes. Below the minimum pressure at which an isobaric section intersects the quadruple point, the T-X diagrams consist of a simple continuous solid/gas, sublimation/condensation envelope. Between these points the discussion given in the sections cited applies. Below the minimum L_I L_{II} critical point C_p the T-X isobaric diagrams all involve the vapor phase in three phase solid/liquid/vapor or liquid$_I$/liquid$_{II}$/vapor reactions, but these are not of sufficient interest

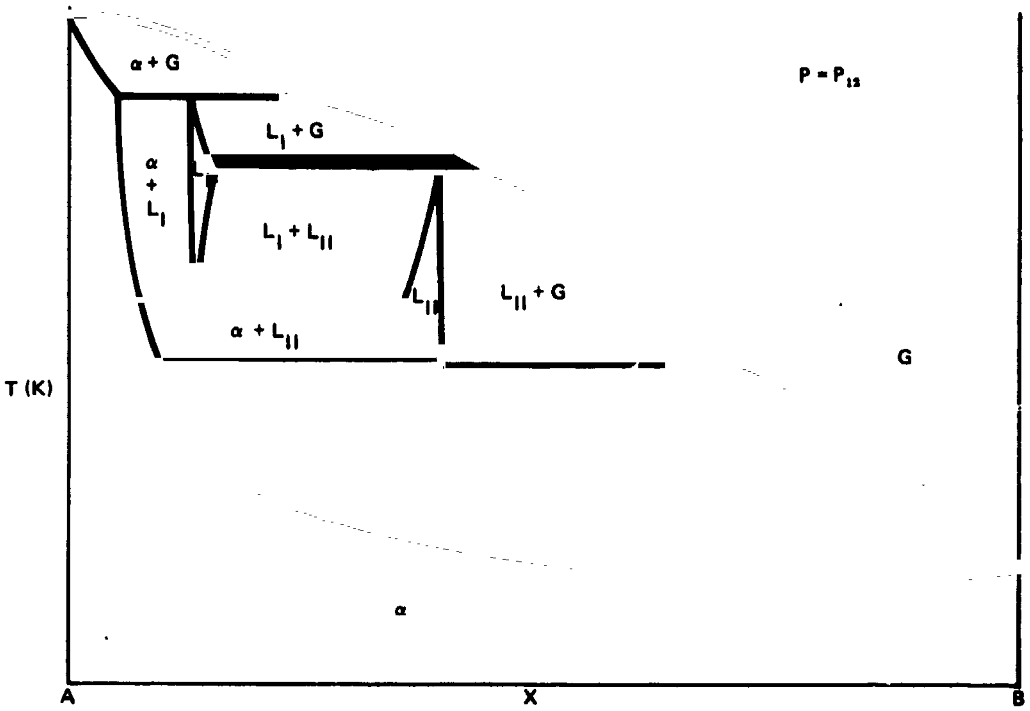

(a) T-X Diagram at P_{12} of Fig. 16b

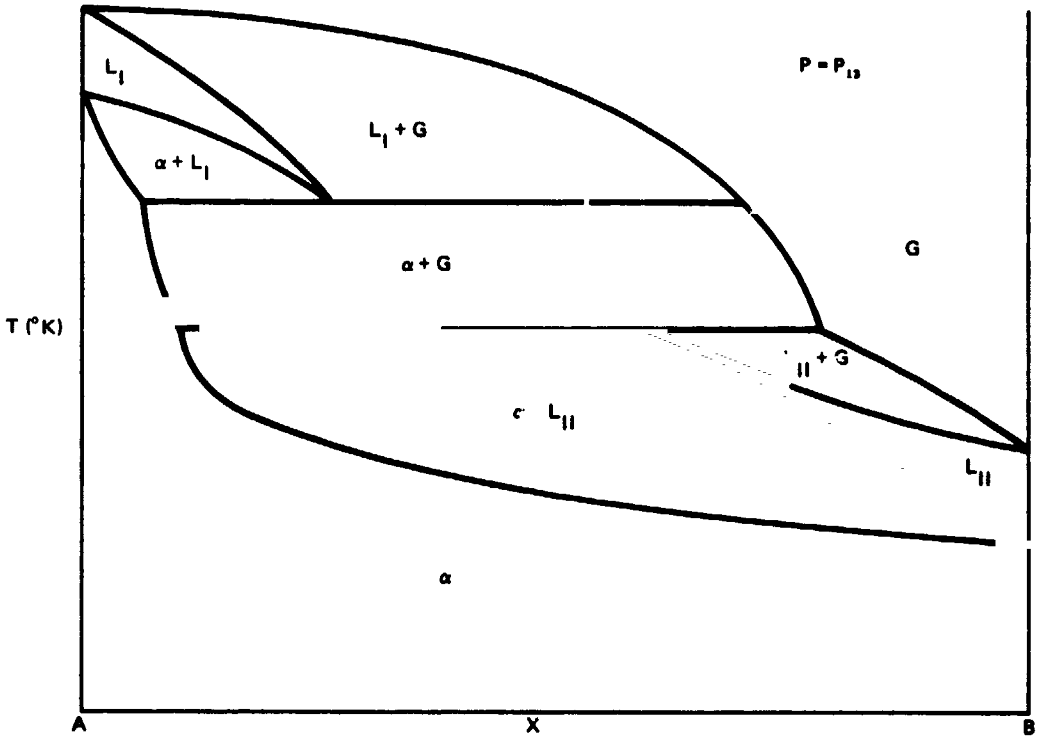

(b) T-X Diagram at P_{13} of Fig. 16c

Fig. 18 Isobaric Sections Involving Cavitation (from Figs 16b and 16c) to be included here since they are only transient during solidification and result in a "cored" structure similar to a normal isomorphous alloy.

Maxima or minima in the GL α line (known as "flexing") as in Fig. 16b can result in cavitative reactions during solidification for both cases shown in Fig. 19. For Case A shown in Fig. 19a, an upward "flex" of the line between Q_A and Q_B will result in a T-X diagram similar to Fig. 18a and will occur in a pressure range between the pressures of P_{QB} and P_H. A downward "flex" where P_H drops below P_{QA} in Fig. 19a will result in a T-X similar to Fig. 18b. Similar results are encountered by "flexing" the Case C GLα line (Fig. 19b) upwards and downwards.

In summary, we may say that cavitative reactions during solidification may be anticipated when the quadruple point H falls on the GLα line of Class B isomorphous systems and when the experimental pressure falls between P_{QA} and P_H or P_H and P_{QB} (if $P_{QB} > C_p$) or P_H and P_{Cp} (if $P_{Cp} > P_{QB}$). Otherwise, special conditions must be contrived to create this sequence of events, such as the "flexing" of three phase lines in pressure-temperature space.

<u>Syntectic</u>

A syntectic reaction is:

$$L_I + L_{II} \rightleftarrows \alpha \qquad (13)$$

and is shown as a T-X diagram in Fig. 20. Projection of this immiscible volume in P-T space is almost analogous to the "sail" in Fig. 15c and because of the temperature maxima of the miscibility gap, the quadruple point H intersects the GLα curve above the melting point of both of the constituent species. This is shown for isomorphous Case B in Fig. 21a.

Consideration of the various isobaric sections, P_1-P_6, indicates that only at the pressure range typified by P_4 do cavitative reactions occur. These reactions are shown in Fig. 21b. Liquid II decomposes to α and a gas, and this is equivalent to Eq. 10.

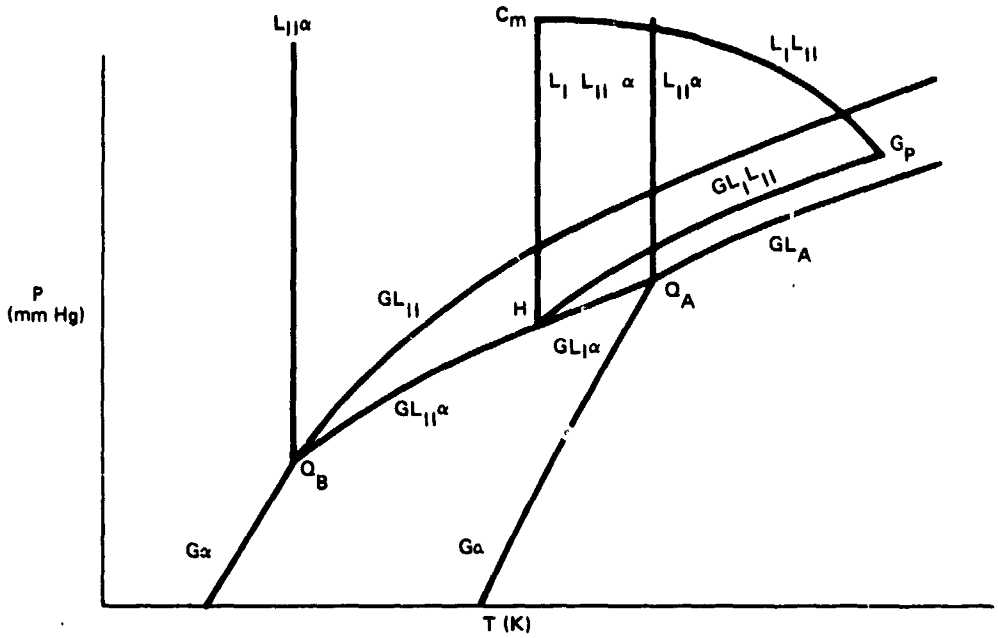

a) Monotectic Reaction of Case A Class

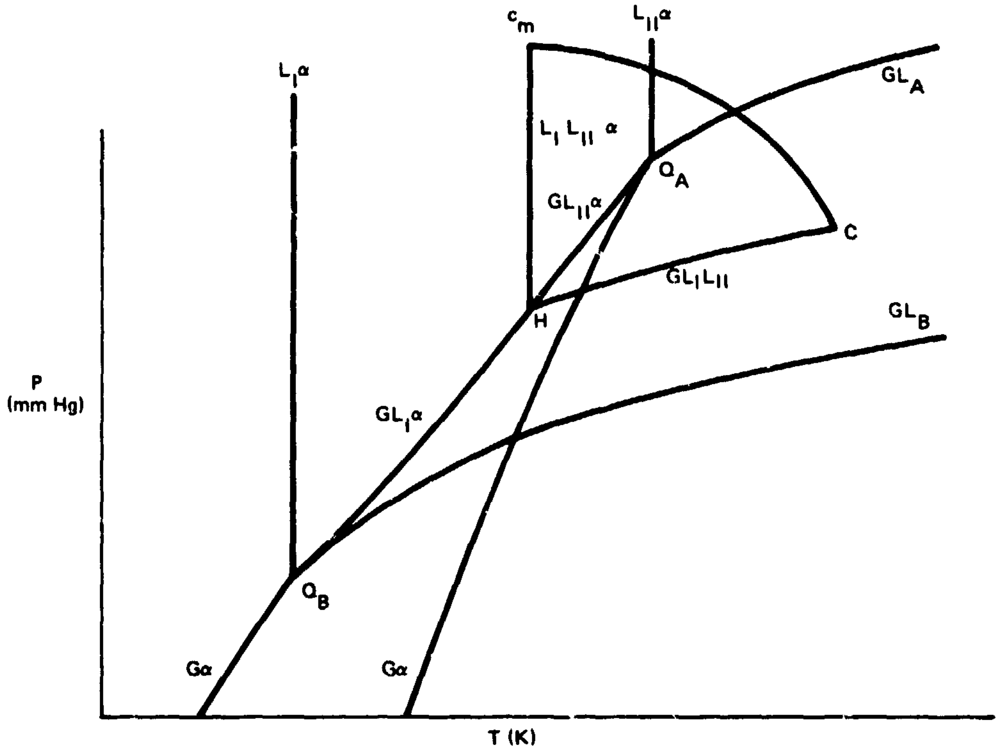

b) Monotectic Projections of Case C Class

Fig. 19 Pressure-Temperature Projections for Monotectic Reactions of Case A and C

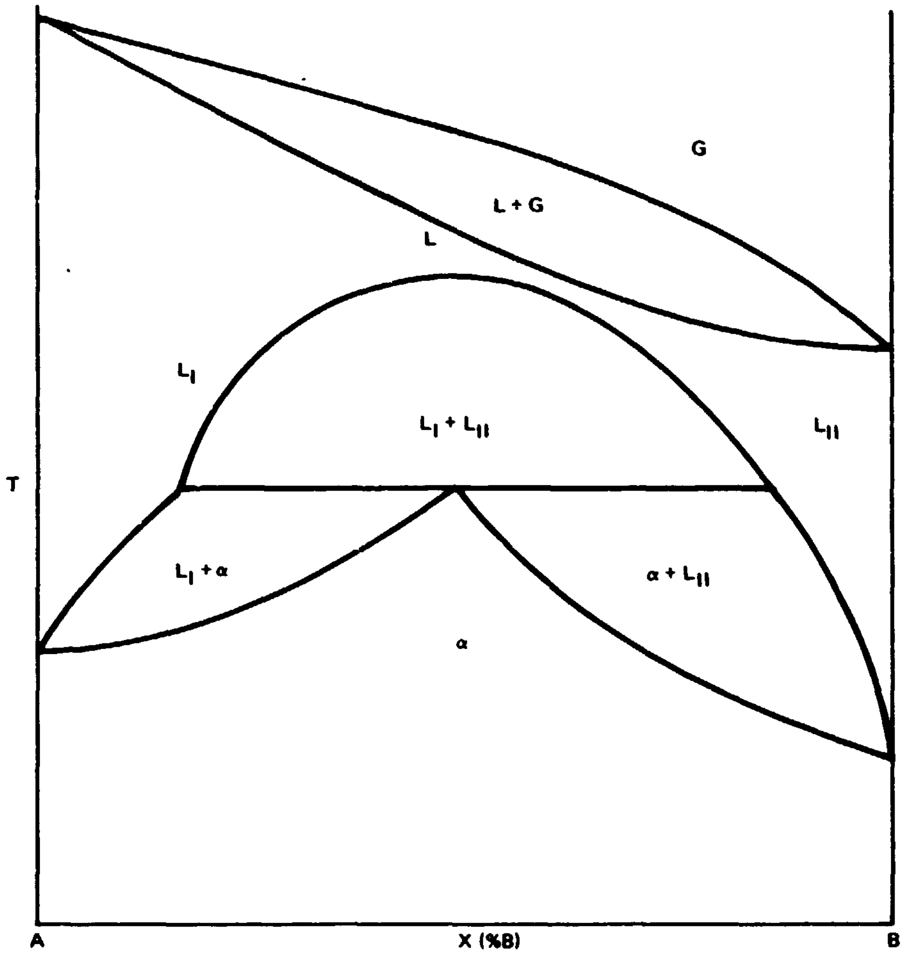

Fig. 20 Syntectic Temperature Composition Diagram (T-X) for the System A-B

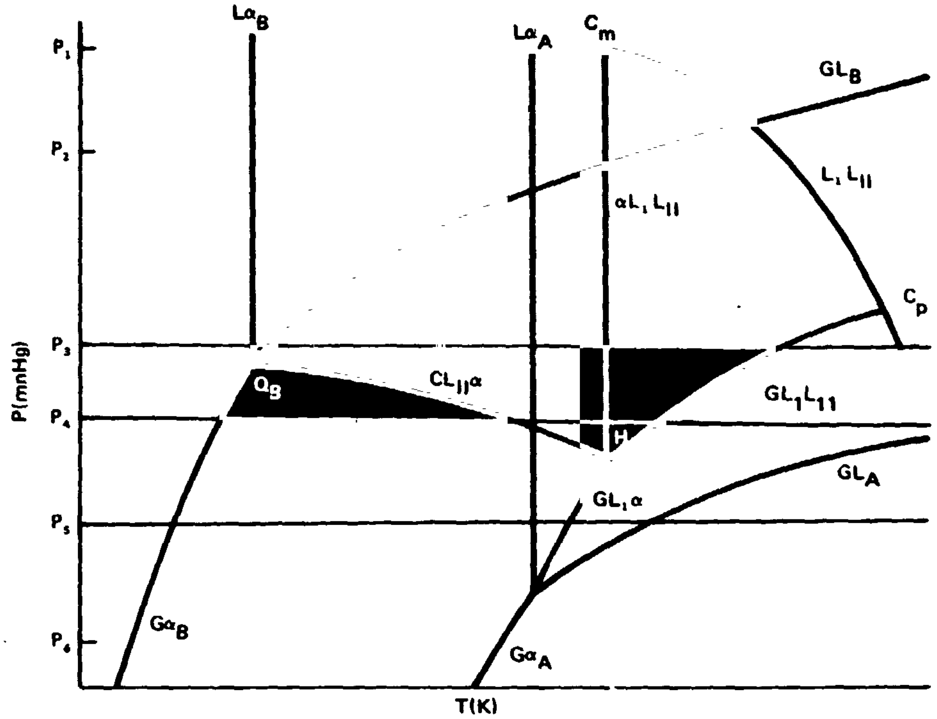

a) P-T Projection for Syntectic System A-B

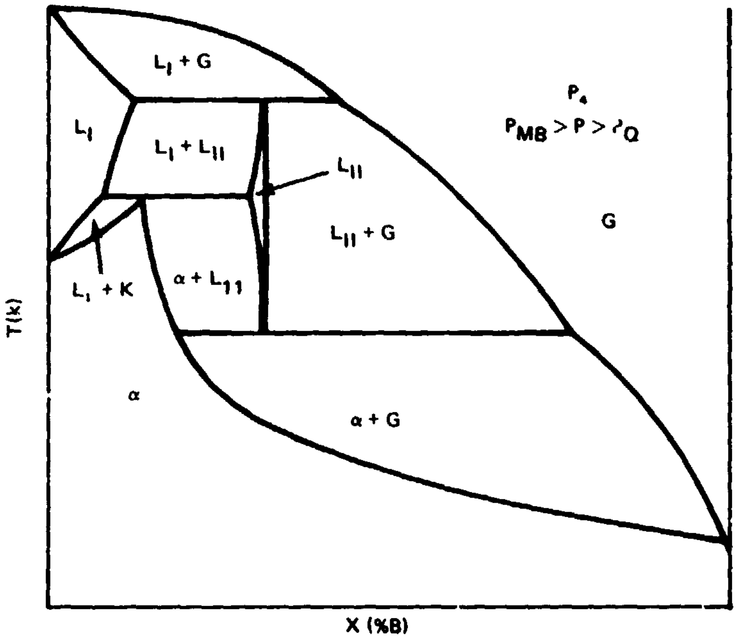

b) Isobaric Section at $P = P_4$

Fig. 21 Pressure-Temperature Projection and Isobaric Section at P_4 for a Syntectic System

Because of the location of the projection of the region of liquid/liquid immiscibility above both T_{QA} and T_{QB}, the primary considerations, as far as cavitation on heating, are those encompassed in the superheat considerations described previously. The balance of the cavitative reactions occur only on superheating.

"Flexing" the location of the quadruple point once again creates singular cavitative reactions on cooling, or cavitation reactions on heating that might occur below the absolute melting point of the highest melting component of a binary alloy, but this is a complexity not predictable from vapor pressure data. Only direct experimental evidence would reveal this.

CONCLUSIONS

Even for the simplest systems of elemental or isostructural solids, the effects of gravity reduction and concomitant pressure reduction are both dramatic and widespread. They should occur in numerous systems; they will make available new controllable solidification reactions to the metallurgist; and they will result in morphologies that can be fabricated only in the orbital environment. These are intriguing prospects, but what is most dramatic about these possibilities is that in most cases they can be evaluated beforehand with accuracy. In general, new cavitative solidification reactions occur in systems that meet the following criteria:

$$T_{QB} > T_{QA},\ P_{QB} < P_{QA} \text{ and } P_{QB} < P_{GL_A} \text{ at } T_{QB}$$

There are cautionary aspects of this work, as well. Unplanned and unwanted cavitation occurring on superheating or below the melting point of one of the constituent elements could be encountered if this analysis is not taken into account in planning future low-g experiments. Figure 1 graphically demonstrates the macroscopic distortion that could occur due to one of the reactions. If this occurred during casting or precise measurement of physical properties, the results would be disastrous. This is no cause for despair, however, as avoidance of these reactions is readily accomplished. It is the implementation of a four-fold increase in the number of controllable solidification reactions that should be emphasized, and to do so must be considered a challenge of the first magnitude. Second phase bubble dispersions have been shown to be effective in retarding high temperature creep (Ref. 5). Porous structures could be created with extremely high specific strengths or moduli (Ref. 6). These controlled arrays are theoretically possible and demonstrable in model solid/liquid/vapor systems. Other specific usages will be presented in Part 2 on two phase solids.

The controlled array of bubbles, however, is not the only potential area of implementation. The absence of buoyancy forces in orbit also makes controlled solidification of liquid/liquid arrays feasible both geometrically and from the standpoint of unique morphological combinations of disparate materials. Unique electronic, thermal, mechanical, and magnetic materials can be predicted and fabricated.

ACKNOWLEDGEMENTS

The author would like to acknowledge the substantial contributions of Dr. J. Papazian, Dr. G. Geschwind, and Mr. W. Aubin to this effort. Without the support and contributions of these individuals, this effort would have been far less productive.

REFERENCES

1. Larson, D. J., Jr., "Specimen Analysis of Skylab, M553 Experiment, Flight Specimens," Final Report on Phase C, Grumman Research Department Report RE-486, August 1974.
2. Larson, D. J. Jr., "Investigation of Ground Base Simulation Skylab Samples," Grumman Research Department Memorandum RM-576, August 1973.
3. Chang, C.E. and Wilcox, W. R., "Inhomogeneities Due to Thermocapillary Flow in Floating Zone Welting," Presented at the First International Colloquium on Drops and Bubbles, Pasadena, Cal., August 1974.
4. Rhines, F. N., Phase Diagrams in Metallurgy, Their Development and Application, McGraw-Hill Book Company, Inc., New York.
5. Sell, H.G. and Stickler, R., "Strengthening Metal with Bubbles," Westinghouse Engineer, Vol. 32, No. 1, pp. 14-18, January 1972.
6. Sell, H.G. and King, G.W., "Bubble Strengthening - A New Materials Concept," Research/Development, Vol. 23, No. 7, pp. 18-21, July 1972.
7. Nesmeyanov, A. N., Vapor Pressure of the Chemical Elements, Elsevier Publishing Co., New York, 1963.
8. Hultgren, R., et al, "Selected Values of the Thermodynamic Properties of the Elements," American Society for Metals, 1973.

APPENDIX

DERIVATION OF THE DEPENDENCE OF THE HYDROSTATIC PRESSURE HEAD UPON POSITION WITHIN A LIQUID SPHERE OF MAXIMUM RADIUS R_o

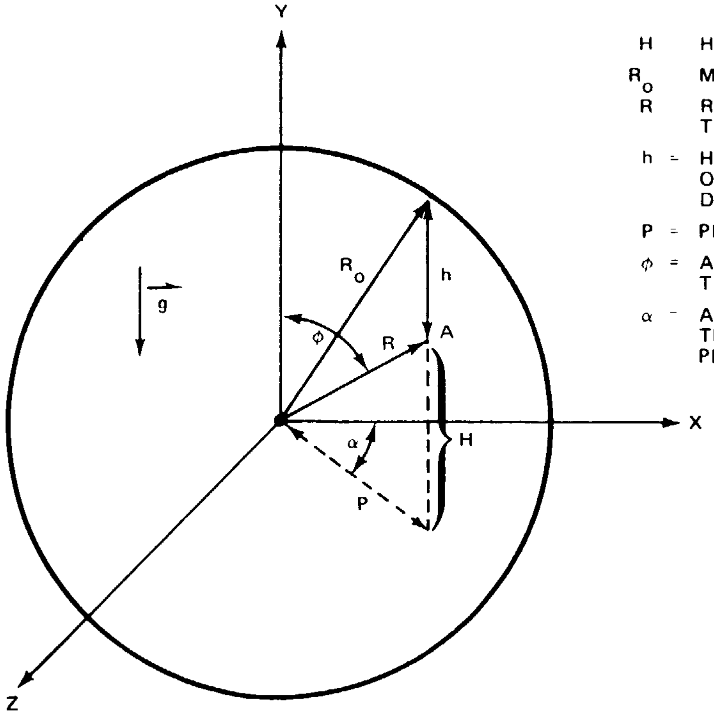

H	HEIGHT ABOVE X, Z PLANE
R_o	MAXIMUM RADIUS OF THE SPHERE
R	RADIUS TO POINT OF INTEREST FROM THE ORIGIN
h =	HEIGHT OF LIQUID ABOVE THE POINT OF INTEREST, IN THE GRAVITATIONAL DIRECTION
P =	PROJECTION OF R IN THE X, Z PLANE
ϕ =	ANGLE BETWEEN THE Y AXIS AND THE RADIUS R
α =	ANGLE BETWEEN THE X AXIS AND THE PROJECTION OF R IN THE X, Z PLANE

NOTE h IS INDEPENDENT OF α BECAUSE OF THE ROTATIONAL SYMMETRY ABOUT THE Y AXIS. THE Y AXIS IS PARALLEL TO g, THE GRAVITY VECTOR.

$$R_o^2 = P^2 + (H + h)^2$$

but $P = R \cos (90^\circ - \phi)$ AND $H = R \sin (90^\circ - \phi)$

then $R_o^2 = R^2 \cos^2 (90^\circ - \phi) + (h + R \sin [90^\circ - \phi])^2$

$$[R_o^2 - R^2 \cos^2 (90^\circ - \phi)]^{1/2} = h + R \sin (90^\circ - \phi)$$

$$h = [R_o^2 - R^2 \cos^2 (90^\circ - \phi)]^{1/2} - R \sin (90^\circ - \phi)$$